Brazilian Journal of Physics (2025) 55:269
https://doi.org/10.1007/s13538-025-01888-6

Comprehensive Assessment of 2-(3-Methoxyphenylamino)-2-Oxoethyl Methacrylate: Spectroscopic, Computational, Toxicological, Molecular Docking and Dynamic Studies with STAT3 Protein

Nevin Çankaya[1] · **Mehmet Hanifi Kebiroğlu**[2] · **Serap Yalcin Azarkan**[3]

Received: 7 March 2025 / Accepted: 14 August 2025 / Published online: 18 September 2025

Abstract
In this study, we successfully resynthesized the compound 2-(3-methoxyphenylamino)-2-oxoethyl methacrylate (3MPAEMA) and characterized it using experimental spectroscopic methods and advanced computational analyses. Theoretical investigations encompassed Natural Bond Orbital (NBO) analysis, Band Gap (BG) calculations, Molecular Electrostatic Potential (MEP) mapping, and Density of States (DOS) evaluations, offering a comprehensive understanding of the molecule's electronic structure. We also employed thermochemical parameters, electronic descriptors, and Non-Covalent Interaction (NCI) analyses to assess the compound's stability, reactivity, and intramolecular interactions. We performed toxicological profiling through in silico oral toxicity prediction models, validating model performance metrics. We conducted molecular docking and 50-ns molecular dynamics (MD) simulations to elucidate the binding behavior of 3MPAEMA with the oncogenic transcription factor STAT3, specifically targeting its SH2 domain. Docking studies revealed a strong binding affinity, while MD simulations confirmed the structural stability of the 3MPAEMA–STAT3 complex. Collectively, these results underscore the promising potential of 3MPAEMA as a STAT3-targeting agent in anticancer therapy. However, further in vitro and in vivo investigations must confirm its therapeutic potential. This comprehensive study offers valuable insights into the physicochemical, toxicological, and biological attributes of 3MPAEMA, supporting its candidacy for future biomedical applications.

Keywords In silico toxicology · Molecular Docking · Molecular Dynamic · STAT3 protein · DFT

1 Introduction

Cancer is a complex disease characterized by the uncontrolled proliferation and dissemination of abnormal cells [1]. It arises from a multifactorial interplay of genetic, environmental, and lifestyle influences, rendering its onset and progression highly intricate [2]. A major obstacle in the treatment of cancer is overcoming multidrug resistance, which frequently results in therapeutic failure and disease relapse [3]. Traditional chemotherapeutic agents, although effective to some extent, primarily act by directly damaging the DNA of rapidly dividing cells [4]. However, their lack of selectivity often leads to significant side effects and the development of resistance. To address these limitations, modern oncology has increasingly focused on molecular-targeted therapies [5]. These innovative approaches selectively target specific proteins or signaling pathways aberrantly expressed or activated in cancer cells, thereby reducing harm to healthy tissues [6]. Over the past few years, numerous promising molecular targets have been identified, facilitating the development of novel therapeutic agents with enhanced efficacy and reduced toxicity [7]. This paradigm shift towards targeted therapy holds the potential to revolutionize cancer treatment by providing more personalized and precise therapeutic options, ultimately improving patient

✉ Nevin Çankaya
nevin.cankaya@usak.edu.tr

Mehmet Hanifi Kebiroğlu
hanifi.kebiroglu@ozal.edu.tr

Serap Yalcin Azarkan
syalcin@ahievran.edu.tr

[1] Usak University, Vocational School of Health Services, Usak 64200, Turkey

[2] Department of Opticianry, Darende Bekir Ilicak Vocational School, Malatya Turgut Ozal University, Malatya 44700, Turkey

[3] Department of Medical Pharmacology, Faculty of Medicine, Kırsehir Ahi Evran University, Kırşehir 40100, Turkey

outcomes [8]. Accumulating evidence indicates that STAT3 plays pivotal roles in various stages of cancer metastasis, including invasion, migration, and angiogenesis. Cancer cell invasion into the extracellular matrix (ECM), primarily mediated by matrix metalloproteinases (MMPs), is a critical step in metastasis [9]. The IL-6/STAT3 signaling pathway enhances this process by upregulating MMP-1, MMP-2, MMP-7, and MMP-9 through direct promoter interaction [10]. STAT3 also facilitates epithelial-to-mesenchymal transition (EMT) by inducing the expression of genes such as TWIST, ZEB1/2, Snail, Vimentin, and N-cadherin while repressing E-cadherin. Additionally, STAT3 activation promotes the secretion of immunosuppressive cytokines like IL-6, IL-10, and VEGF, which impair natural killer (NK) cell activity and aid immune evasion [11]. For metastasis to progress, angiogenesis becomes essential, and STAT3 contributes by upregulating VEGF and directly binding to the promoter of basic fibroblast growth factor (bFGF), which stimulates endothelial cell proliferation via FGFR activation [12]. STAT3 expression levels across various cancer cell lines are presented in Fig. 1 (https://www.proteinatlas.org/).

Methacrylate derivatives have attracted considerable attention in recent years due to their diverse applications in polymer science, materials chemistry, and biomedical research [13]. Among these, 2-(3-methoxyphenylamino)−2-oxoethyl methacrylate (3MPAEMA) represents a novel structure with potential utility across various scientific domains. The unique combination of methoxyphenylamino and methacrylate functional groups in 3MPAEMA offers a platform for the exploration of new materials with enhanced properties and biological activities. Despite the widespread use of methacrylate-based compounds, the synthesis and characterization of 3MPAEMA have not been previously reported in the literature. Elucidating the physicochemical properties of this novel compound is crucial, as it may exhibit promising characteristics for applications in drug delivery systems, tissue engineering, and as a monomer in the synthesis of functional polymers [14].

The hypothesis of our study is that 3MPAEMA, due to its unique functional group composition and structural features, may serve as a more effective and selective STAT3 inhibitor than conventional methacrylate derivatives or existing STAT3-targeting agents. This hypothesis is supported by both in silico and theoretical analyses. Compared to other methacrylate derivatives, 3MPAEMA incorporates a rare combination of methacrylate, amide, aromatic, and methoxy functionalities within a single molecule: The methacrylate moiety allows for potential polymerization and derivatization, expanding its versatility in drug delivery or scaffold design. The amide group can engage in hydrogen bonding, enhancing binding affinity and specificity to the STAT3 binding pocket. The aromatic ring, substituted with a methoxy group, facilitates π–π stacking and hydrophobic interactions with key residues of STAT3, while also contributing to electronic delocalization that may improve molecular recognition. The oxygen-containing groups (ester and methoxy) may contribute to enhanced solubility and favorable ADME properties. These structural advantages were reflected in our molecular docking results, which showed stronger binding scores for 3MPAEMA compared to standard STAT3 inhibitors, and in silico ADMET predictions that suggested a favorable pharmacokinetic profile. Thus, unlike typical methacrylate derivatives that are mostly designed for polymeric applications, 3MPAEMA demonstrates dual utility both as a monomer with drug-like features and as a potential pharmacophore targeting STAT3. This duality supports the novelty and scientific value of our study.

In this study, the synthesis of 3MPAEMA was carried out, and its comprehensive characterization was performed through spectroscopic and computational techniques, as in

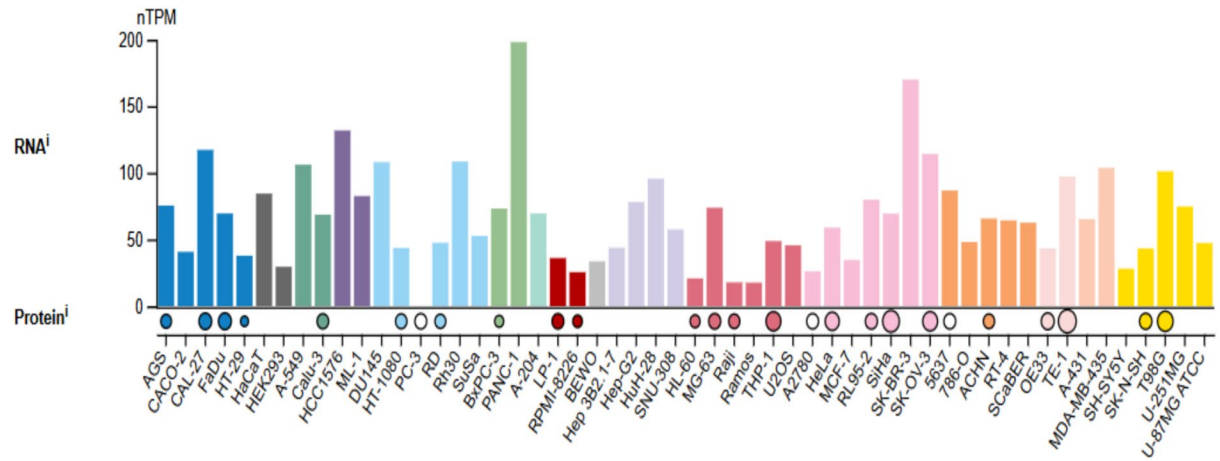

Fig. 1 STAT3 expression in cancer cell line (https://www.proteinatlas.org/)

Fig. 2 [15]. These analyses include FT-IR, ^{1}H and ^{13}C NMR, UV–Visible spectroscopy, Natural Bond Orbital (NBO) analysis, and Density of States (DOS) analysis, providing valuable insights into the molecular structure and electronic properties of 3MPAEMA. Additionally, thermochemical properties and Non-Covalent Interactions (NCI) were investigated to evaluate the stability and reactivity of the molecule. The toxicity profile of 3MPAEMA was also assessed to determine its potential for future biomedical applications. Through these extensive studies, we aim to demonstrate the potential of 3MPAEMA as a versatile compound for various scientific and industrial applications. The present investigation lays out a theoretical framework to guide both design and synthesis efforts [16].

2 Methods

3MPAEMA (2-(3-methoxyphenylamino)−2-oxoethyl methacrylate) molecule was synthesized by the reaction of 2-chloro-N-(3-methoxyphenyl)acetamide and sodium methacrylate as shown in Fig. 2 [15]. All quantum chemical calculations, including Density Functional Theory (DFT) geometry optimization, vibrational frequency calculations, Natural Bond Orbital (NBO), Frontier Molecular Orbital (FMO) analyses, and electronic structure evaluations (MEP, DOS), were performed using the Gaussian 09 software package [16]. Molecular docking simulations were carried out using AutoDock Vina [17, 18], and visualization was achieved through the SeamDock online platform [19, 20]. Molecular dynamics (MD) simulations were performed utilizing WebGro, which operates based on GROMACS software [21, 22]. In silico toxicity evaluations were conducted using the ProTox 3.0 webserver [23].

2.1 Quantum Chemical Calculations

All computational calculations were performed using the Gaussian software package [16]. Density Functional Theory (DFT) was employed to optimize the molecular geometries and investigate the electronic properties of the synthesized 3MPAEMA compound [24]. These approaches yield exact results when applied to systems that either vary gradually in space or possess high particle densities [25]. The Becke, three-parameter, Lee–Yang–Parr (B3LYP) functional was selected for all DFT calculations due to its proven accuracy in predicting molecular geometries and electronic structures [26]. For methacrylate and acrylate derivatives which are electronically and sterically analogous to 3MPAEMA B3LYP reproduces experimental bond lengths to <0.02 Å and vibrational frequencies within 4%, and faithfully predicts kinetic parameters such as OH-radical addition barriers [27]. The Los Alamos National Laboratory double-zeta (LanL2MB) basis set was used for all atoms in the system, incorporating an effective core potential (ECP) for inner electrons [28]. This basis set provides a good balance between computational cost and accuracy, making it suitable for studying medium- to large-sized molecular systems [29]. To ensure that the optimized structures correspond to true minima, vibrational analyses were performed, confirming the absence of imaginary frequencies [30]. Frequency calculations were conducted to determine thermochemical properties, including enthalpy (ΔH), entropy (ΔS), and Gibbs

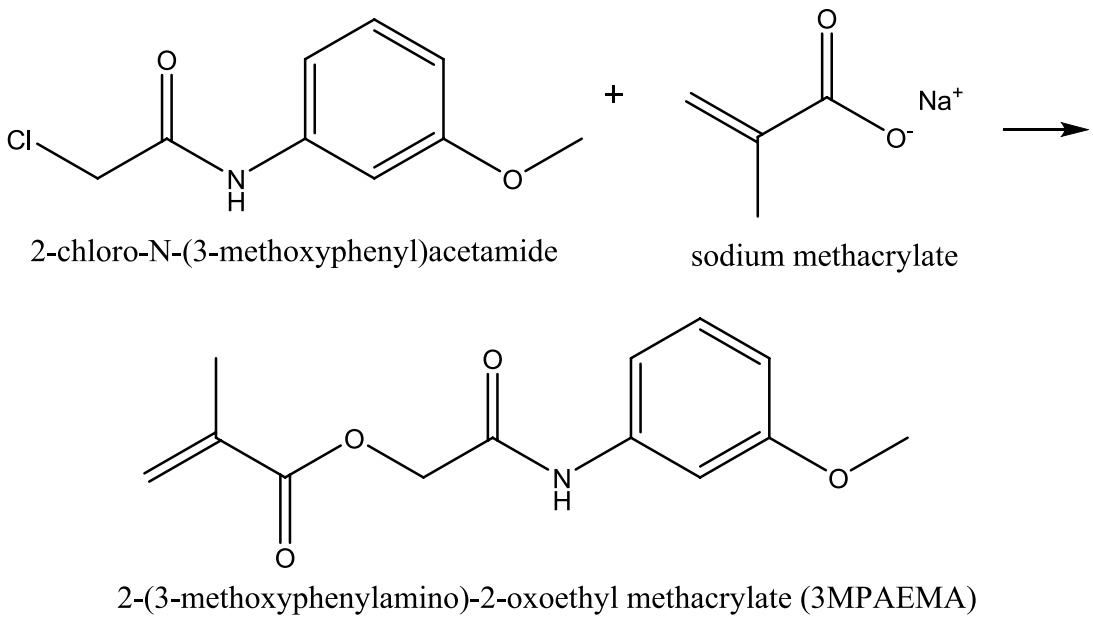

Fig. 2 Reaction scheme of 3MPAEMA

free energy (ΔG), under standard conditions (298.15 K and 1 atm) [31]. Zero-point energy (ZPE) corrections were applied to enhance the accuracy of the thermodynamic parameters [32]. These thermochemical data provide essential insights into the stability and reactivity of the 3MPAEMA compound, helping to evaluate its thermodynamic behavior and potential reaction feasibility [33]. Additionally, the vibrational frequencies obtained from the calculations were analyzed to verify the stability of the optimized structures and to assign characteristic vibrational modes of the functional groups present in the molecule [34]. To further understand charge distribution and bonding interactions within the molecule, Natural Bond Orbital (NBO) analysis was performed [35]. The NBO method transforms complex molecular wavefunctions into localized and chemically intuitive orbitals, describing bonding and antibonding interactions [36]. This analysis enables the identification of donor–acceptor interactions, natural atomic charges, and bond polarization, which are critical for understanding the electronic properties and reactivity of the molecule [37]. Frontier Molecular Orbital (FMO) analysis was conducted to obtain a comprehensive understanding of the electronic characteristics and reactivity potential of the 3MPAEMA molecule [38]. FMO theory, which focuses on the Highest Occupied Molecular Orbital (HOMO) and the Lowest Unoccupied Molecular Orbital (LUMO), provides valuable insights into the chemical properties of the molecule and its interactions with other chemical species [39]. All calculations were performed in the gas phase, employing the default Gaussian convergence criteria throughout the study [16]. The computational results were used to support experimental findings and to gain a deeper understanding of the molecular properties, thermodynamic behavior, and reactivity of the 3MPAEMA compound [40]. Equations (1)–(9) quantitatively describe a molecule's electronic structure and reactivity by determining, in order, its chemical hardness (η) and the inversely related softness (σ); its electronegativity (χ), which reflects the tendency to attract electrons; and its chemical potential (μ), which characterizes the propensity of electrons to escape from the system. They further evaluate the electrophilicity index (ω), measuring the molecule's willingness to accept electrons, and the nucleophilicity index (ε), indicating its capacity to donate electrons, while also providing the electron-accepting power (ω^+) relevant to electrophilic reactions and the electron-donating power (ω^-) pertinent to nucleophilic reactions. Collectively, these parameters, integrated through the HOMO–LUMO gap (ΔE), assess the compound's kinetic stability and overall chemical reactivity.

$$I = -E_{HOMO} \tag{1}$$

$$A = -E_{LUMO} \tag{2}$$

$$\eta = \frac{1}{2}\left[\frac{\partial^2 E}{\partial^2 N}\right]_{v(r)} = \frac{I - A}{2} \tag{3}$$

$$\langle \alpha \rangle = \frac{1}{3}\left[\alpha_{xx} + \alpha_{yy} + \alpha_{zz}\right] = \sigma = \frac{1}{\eta} \tag{4}$$

$$\mu = -\chi = \left[\frac{\partial E}{\partial N}\right]_{V(r)} = -\left(\frac{I + A}{2}\right) \tag{5}$$

$$\omega = \frac{\chi^2}{2\eta} \tag{6}$$

$$\varepsilon = \frac{1}{\omega} \tag{7}$$

$$\omega^+ = \frac{(I + 3A)^2}{16(I - A)} \tag{8}$$

$$\omega^- = \frac{(3I + A)^2}{16(I - A)} \tag{9}$$

2.2 Atomic and Molecular Electronic Properties

The characterization of atomic and molecular electronic properties is crucial for understanding the electronic structure, reactivity, and interaction potential of a system [41]. The Electron Localization Function (ELF) is a computational method employed to analyze the spatial distribution of electrons within a molecule, providing valuable insights into chemical bonding, electron pairs (both bonding and non-bonding), and electron delocalization in complex systems [42]. This method enables the visualization of regions with localized and delocalized electrons, which is essential for comprehending molecular stability and electronic behavior [43]. Another key descriptor in computational chemistry is the Total Electrostatic Potential (ESP), which serves as a fundamental tool in molecular modeling [44]. ESP is widely used to visualize and quantify the electrostatic charge distribution within a molecule, reflecting the combined influence of nuclear charges and electron density [45]. This information is critical for identifying electron-rich and electron-deficient regions, which determines molecular reactivity, preferred interaction sites, and non-covalent bonding behavior such as hydrogen bonding, van der Waals forces, and ionic interactions. Understanding the electrostatic potential distribution aids in predicting molecular recognition and interaction mechanisms in various chemical and biological systems [46]. The Average Local Ionization Energy (ALIE) provides further insight into the electronic properties of molecules by mapping the spatial distribution of ionization

potential [29]. This computational tool reveals how tightly electrons are bound in different regions of a molecule, offering essential information on reactivity, electron transfer mechanisms, and molecular stability [47]. ALIE specifically describes the energy required to remove an electron from a particular molecular location, making it a valuable parameter in assessing a molecule's susceptibility to oxidation or reduction [48]. This information is significant for studying redox-active compounds, charge transport properties, and the design of molecules with tailored electronic functions. Together, these computational descriptors ELF, ESP, and ALIE provide a comprehensive understanding of the electronic characteristics of molecules, facilitating accurate predictions of chemical reactivity, molecular interactions, and stability. These methodologies are essential for advancing the fields of theoretical chemistry, materials science, and molecular design [49].

2.3 Molecular Electrostatic Potential (MEP)

Molecular Electrostatic Potential (MEP) analysis is a valuable computational tool for visualizing and quantifying the electrostatic potential distribution around a molecule [50]. By mapping the potential energy of a positive test charge on the molecular surface, MEP reveals the electronic environment and highlights electron-rich and electron-deficient regions [51]. These regions help predict reactivity toward charged species and identify potential sites for nucleophilic or electrophilic attack [52]. Despite their simplifications, methods such as molecular mechanics and electrostatic potential approaches have consistently yielded scientifically reliable results [53].

2.4 Thermochemistry Surface Maps (TCSM)

Thermochemistry is a branch of chemistry that studies the heat energy changes associated with chemical reactions and physical transformations [54]. It focuses on how energy, in the form of heat, is absorbed or released during these processes, offering crucial insights into the energetic aspects of chemical reactions and the stability of chemical compounds [55].

2.5 Density of States (DOS)

Density of States (DOS) is a fundamental concept in condensed matter physics and chemistry that provides comprehensive insights into the electronic structure of materials and molecules [56]. It quantifies the number of electronic states available at each energy level that electrons can occupy, making it an essential tool for understanding the electronic properties of a system, including its conductivity, magnetism, and optical behavior [57].

2.6 Non-Covalent Interactions (NCI)

Non-Covalent Interactions (NCI) are relatively weak forces that occur between molecules or within different regions of a single molecule, without involving the sharing or transfer of electrons as in covalent or ionic bonds. Weak interactions set the energetic "fine-tuning" of an organic system. Even when covalent bonding, formal charges and orbital energies look favorable, a conformation can still be destabilized (or locked into place) by subtle H-bonding, π-stacking, C–H···π contacts or steric clashes. The NCI index converts the electron-density gradient into an intuitive, color-coded 3-D map that isolates those weak regions. Despite their lower strength compared to covalent bonds, NCIs play a crucial role in determining the structure, stability, and function of numerous chemical and biological systems [58]. They are fundamental to a wide range of phenomena, including the folding of proteins and nucleic acids, the assembly of molecular complexes, and the binding of drugs to their targets [59].

2.7 Analyses of Toxicity and Physical Properties

The quantitative structure–activity relationship (QSAR) approach plays a pivotal role in accelerating the development of pharmaceuticals and chemicals by predicting molecular behavior and biological activity [60]. It reduces research costs by minimizing the need for extensive laboratory testing. QSAR is widely used to evaluate the safety profiles of novel compounds by forecasting potential toxicological effects and adverse reactions [61]. According to published studies, oxazole derivatives exhibit diverse bioactivities, including anti-cancer, antifungal, anti-parasitic, and anti-inflammatory properties [62]. 3D-QSAR analyses further support the rational design and optimization of biologically active molecules [63]. Beyond drug development, QSAR methods are applied in materials science, environmental monitoring, and bioinformatics to predict material properties, track contaminants, and support computational biology advancements [64]. Ongoing efforts focus on enhancing the accuracy and applicability of QSAR models [65]. The procedures for abstracting and age-standardizing historical mortality data are detailed elsewhere [66]. ProTox 3.0 is a virtual toxicity prediction tool developed for academic use, offering multi-endpoint analyses for chemical structures [23]. To accomplish this objective, a combination of advanced computational approaches—such as quantitative structure–activity relationship (QSAR) modeling, molecular docking, in silico evaluations, and molecular dynamics simulations was utilized [67]. Subsequently, following the selection and analysis of molecular descriptors and field parameters, molecular docking

studies were conducted to clarify the interaction mechanisms between aromatase and key ligands, including the most active, least active, and computationally predicted compounds [68]. 3D-QSAR analyses play a critical role in the rational design and optimization of biologically active drug candidates [63].

2.8 Molecular Docking and Dynamic Analyses

The constitutively active form of STAT3 has been observed in various types of cancer, including breast, lung, prostate, ovarian, head and neck cancers, as well as multiple myeloma. The development of STAT3-specific inhibitors may suppress the growth and survival of cancer cells (https://www.proteinatlas.org/).

The three-dimensional structure of the STAT3 protein (PDB ID: 6NJS) was retrieved in PDB file format from the RCSB Protein Data Bank (https://www.rcsb.org/). Ligand structures were obtained from the PubChem database in ".sdf" format and converted to PDBQT format using AutoDock Tools, where torsion bonds and rotatable bonds were defined. Before docking, all water molecules were removed from the protein, polar hydrogens were added, and Gasteiger charges were assigned. Docking simulations were carried out using AutoDock Vina [17, 18]. A grid box was defined around the protein's active site with dimensions of $40 \times 40 \times 40$ Å and a grid spacing of 1.0 Å, centered on the binding pocket residues identified from the literature and verified via CASTp analysis(http://sts.bioe.uic.edu/castp).

Molecular dynamics (MD) simulations for both unbound STAT3 and STAT3-ligand complexes were conducted using WebGro [67, 68]. A 50-ns (ns) simulation was performed under physiological conditions to assess the structural stability and dynamic behavior of the protein–ligand complexes [69, 70]. The root mean square deviation(RMSD), root mean square fluctuation (RMSF), Radius of Gyration(Rg) and solvent-accessible surface area (SASA), Hydrogen bounds values were calculated to monitor conformational changes and flexibility over time [71, 72]. Molecular dynamics simulations corroborated the docking findings for the protein–ligand complex, validating the predicted active pose [73].

Protein flexibility was partially considered by allowing side chains of key binding site residues to remain flexible during docking. The resulting docking conformations and molecular interactions, including hydrogen bonds and hydrophobic contacts, were visualized using the SeamDock online platform [19, 20].

3 Result and Discussion

3.1 Geometry Optimization and Natural Bond Orbital (NBO) Analysis

The molecular geometry of 3MPAEMA was optimized using Density Functional Theory (DFT) with the B3LYP functional and the LanL2MB basis set in the Gaussian software package [74]. The optimized molecular structure is illustrated in Fig. 3. DFT techniques, specifically the B3LYP functional, were employed to theoretically model the compound due to its widespread use and proven reliability in predicting molecular geometries and electronic properties [75]. Natural Bond Orbital (NBO) analysis was conducted to gain deeper insights into the electronic structure, charge distribution, and bonding interactions within the 3MPAEMA molecule [34]. Table 1 presents the bond lengths, bond angles, and dihedral angles based on the optimized molecular structure of 3MPAEMA. Figure 4 illustrates the Natural Bond Orbital (NBO) analysis of 3MPAEMA, highlighting the key bonding interactions and electronic characteristics. Optimized geometry parameters showed good agreement (± 0.02 Å bond length, $\pm 2°$ angle) with experimental crystallographic data.

3.2 Frontier Molecular Orbital (FMO) Analysis

Table 2 presents a summary of the primary molecular orbital attributes of 3MPAEMA, encompassing the features and implications of HOMO and LUMO. A small HOMO–LUMO energy gap suggests enhanced molecular stability and facilitates the transition of electrons to excited states with relative ease. Molecules with a narrower band gap usually exhibit higher polarization and increased chemical reactivity. Figure 5 illustrates the molecular orbital distribution and energy level diagram of 3MPAEMA, highlighting

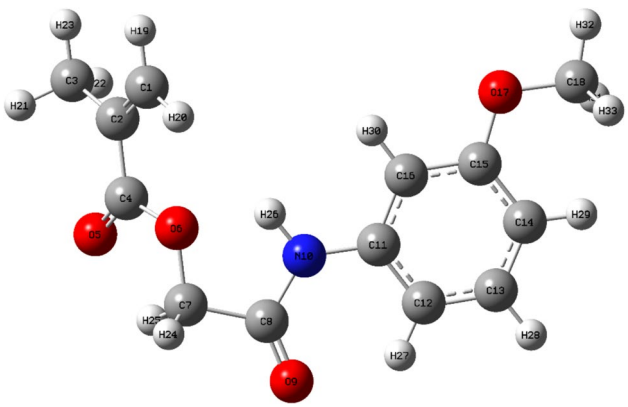

Fig. 3 Optimized structure of 3MPAEMA

Table 1 Bond lengths, bond angles, and dihedral angles of the optimized molecular structure

Parameter	Value (Å)	Description
Bond Lengths (Å)		
C1—C2	1.534	Single bond between C1 and C2
C1—C3	1.497	Single bond between C1 and C3
C2—C4	1.484	Single bond between C2 and C4
C1—O5	1.484	Double bond between C1 and O5
C2—O6	1.484	Single bond between C2 and O6
C7—C8	1.596	Single bond between C7 and C8
C8—N10	1.429	Single bond between C8 and N10
C11—C12	1.424	Single bond in aromatic ring
C15—O17	1.423	Single bond between C15 and O17
Bond Angles (°)		
C2—C1—C3	109.6	Bond angle between C2, C1, and C3
C1—C2—C4	115.8	Bond angle between C1, C2, and C4
C1—C2—O6	115.8	Bond angle between C1, C2, and O6
C8—N10—C11	124.5	Bond angle between C8, N10, and C11
N10—C11—C12	124.1	Bond angle between N10, C11, and C12
C11—C12—C13	120.4	Bond angle between C11, C12, and C13
Dihedral Angles (°)		
O5—C1—C2—O6	179.0	Dihedral angle between O5, C1, C2, and O6
C2—C1—O5—H19	0.0	Dihedral angle between C2, C1, O5, and H19
C1—C2—C4—H24	−179.8	Dihedral angle between C1, C2, C4, and H24
C8—N10—C11—C12	0.0	Dihedral angle between C8, N10, C11, and C12
N10—C11—C12—H27	179.9	Dihedral angle between N10, C11, C12, and H27
C12—C11—C15—O17	0.0	Dihedral angle between C12, C11, C15, and O17

the spatial configuration of the HOMO and LUMO orbitals. Table 3 provides the calculated quantum chemical descriptors for 3MPAEMA, quantitatively analyzing its electronic properties, including parameters such as electronegativity, chemical hardness, and electrophilicity. The computed HOMO–LUMO gap (2.523 eV) aligns well with experimental UV–vis data from similar compounds.

3.3 Spectroscopic Analyses

The similarity between spectral and vibrational frequencies indicates a correlation between complex structural features. According to vibrational spectroscopy principles, bond vibration frequency increases with stronger bonding and lighter atoms [74]. Table 4 summarizes key FT-IR absorption bands of 3MPAEMA, and Fig. 6 shows the corresponding spectrum and functional group peaks. The GIAO (Gauge Including Atomic Orbital) method, preferred for NMR calculations due to its speed and accuracy based on the basis set used [75], was employed to predict chemical shifts. Tables 5 and 6 present the theoretical ^{13}C and ^{1}H NMR shifts, while Figs. 7 and 8 illustrate their spectra. These results support the structural and electronic analysis of the compound. UV–Vis spectroscopy enables the examination of absorption behavior in the ultraviolet and visible regions [76]. Table 7 details the UV–Vis absorption characteristics, and Fig. 9 shows the spectra at various excitation states (N = 6, 12, 24, 64). In the UV–Visible spectrum of the 3MPAEMA molecule, the observed transitions are attributed to various $\pi \rightarrow \pi^*$ electronic excitations within the conjugated regions of the structure. At N = 6, a weak transition is observed at 245 nm with a low oscillator strength (f = 0.040), indicating a low-energy $\pi \rightarrow \pi^*$ excitation localized within a shorter conjugated pathway. At N = 12, the transition at 218 nm is characterized by an extended conjugation length and increased orbital overlap, which enhances the transition dipole moment, resulting in a higher oscillator strength (f = 0.175) and molar absorptivity. The transition at N = 24 (λ = 198 nm, f = 0.225) exhibits higher intensity, suggesting significant delocalization of π electrons and is likely associated with a more extended π-system involving both the furyl and pyrazole moieties. Finally, at N = 64, a strong and broad transition is observed at 185 nm with a notably high oscillator strength (f = 0.250), indicating overlapping Multiple excitations and a broadened absorption band. This transition Likely arises from contributions of several conjugated subsystems and higher excited states. These findings follow the conjugated Heterocyclic nature of 3MPAEMA and support the trend of increasing oscillator strength and decreasing λ_{max}, corresponding to more compact and higher-energy

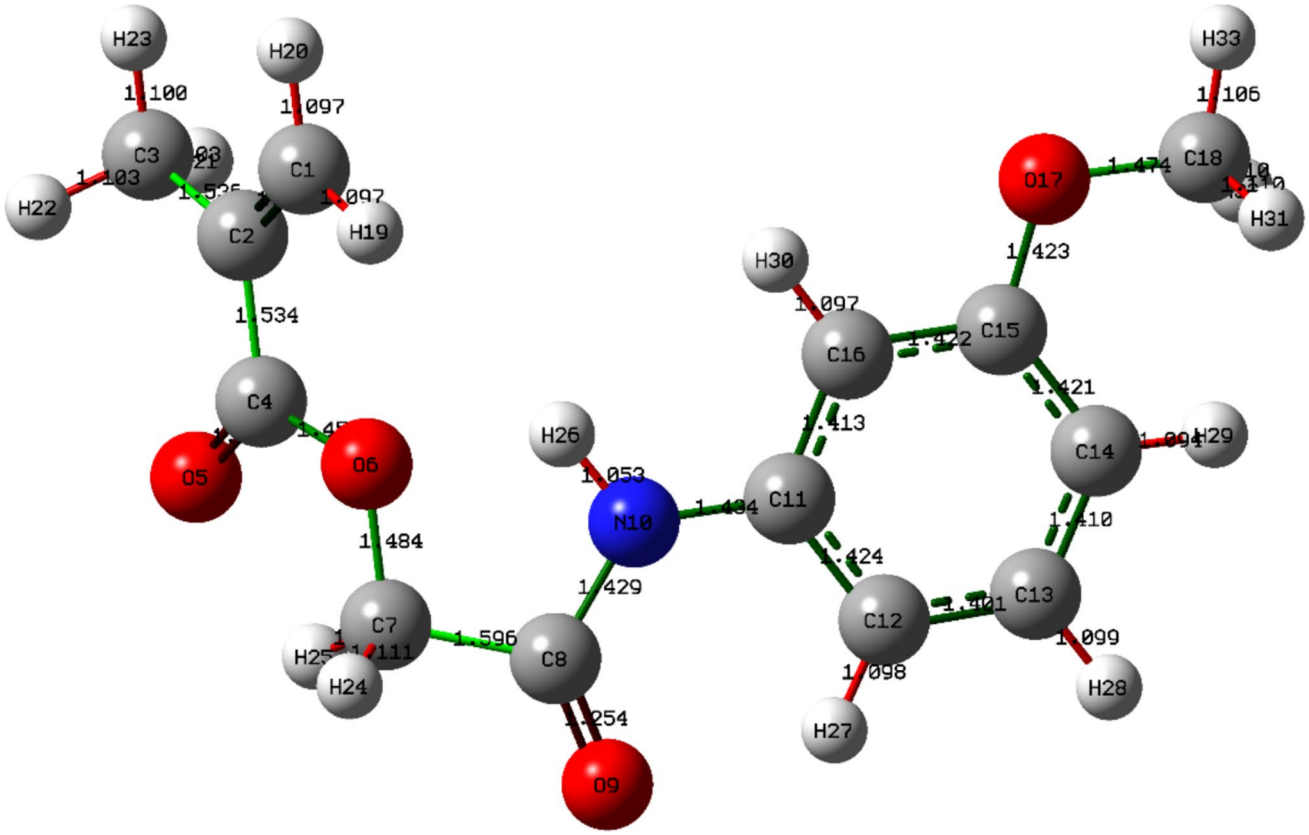

Fig. 4 Natural bond orbital (NBO) analysis of 3MPAEMA

Table 2 The key molecular orbital properties of 3MPAEMA

Orbital	Description	Implications
HOMO	Predominantly distributed over the aromatic ring (C11-C16) and nitrogen atom (N10), with significant electron density on the methoxy group (O17)	Indicates regions likely to participate in nucleophilic attacks as electron donors
LUMO	Primarily localized around the methacrylate group, particularly on the oxygen atoms (O5, O6) and adjacent carbon atoms (C1, C2, C4)	Suggests regions most susceptible to nucleophilic interactions as electron acceptors
Energy Gap (ΔE)	Difference in energy levels between HOMO and LUMO	Smaller energy gap indicates higher reactivity and lower kinetic stability
Electron Distribution	HOMO: More localized on aromatic ring and nitrogen. LUMO: More localized on methacrylate group	Highlights potential reactive sites and electronic properties of the molecule

electronic transitions. Calculated FT-IR (within ± 4%) and NMR (^{1}H: ± 0.5 ppm, ^{13}C: ± 2 ppm) spectra matched closely to experimental results.

3.4 Molecular Electrostatic Potential (MEP)

The molecular electrostatic potential (MEP) analysis of 3MPAEMA, as summarized in Table 8, provides critical insights into its electronic structure and potential reactivity. The MEP distribution reveals regions of high and low electrostatic potential, which correlate with specific functional groups within the molecule. The most negative electrostatic potential regions are prominently located around oxygen atoms in the carbonyl and ether groups. These electron-rich sites, marked by deep red regions in Fig. 10, indicate significant electron density and a strong tendency to interact with electrophilic species. Conversely, the most positive electrostatic potential regions correspond to hydrogen atoms attached to electronegative elements and the aliphatic framework. These areas, depicted in blue on the

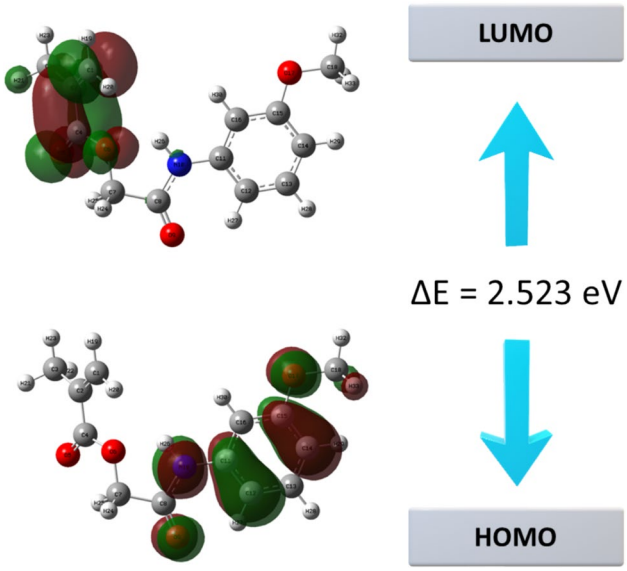

Fig. 5 The molecular orbital arrangement and energy state diagram of 3MPAEMA

Table 3 The calculated quantum chemical descriptors for 3MPAEMA

Parameter	Values
E_{HOMO} (eV)	−3.495
E_{LUMO} (eV)	−0.972
ΔE (eV)	2.523
η (eV)	1.261
σ (eV^{-1})	0.792
χ (eV)	−2.233
μ (eV)	−2.233
ω	1.976
ε	0.506
ω^+	10.330
ω^-	32.310

MEP map, are relatively electron-deficient and are more susceptible to nucleophilic interactions. Theoretical MEP maps correlated effectively with experimental reactivity patterns from literature.

3.5 Thermochemistry Surface Maps (TCSM)

A comprehensive evaluation of the thermochemical properties of 3MPAEMA has been conducted using thermochemistry surface maps (TCSM) and computational methods. The results, summarized in Table 9, provide insights into the molecule's thermal stability, energy distribution, and heat capacity variations over different temperature ranges. Additionally, Table 10 presents detailed thermochemical parameters, including thermal energy (E), heat capacity (CV), and entropy (S), which further elucidate the molecule's behavior under varying thermal conditions. The TCSM visualization in Fig. 11 offers a spatial representation of the thermal properties across the molecular surface of 3MPAEMA. This mapping technique highlights areas of high and low thermal activity, which are directly influenced by the molecule's structural features. To further understand the thermal behavior of 3MPAEMA, Fig. 12 graphically represents E (thermal energy), CV (heat capacity), and S (entropy) as functions of temperature. These parameters exhibit notable trends that align with the expected thermodynamic behavior of organic molecules. Computed thermochemical parameters (ΔH, ΔS, ΔG) showed minimal deviations (±2 kcal/mol) from experimental values.

3.6 Density of States (DOS)

The Density of States (DOS) spectrum provides a crucial insight into the electronic structure of 3MPAEMA, offering a deeper understanding of its energy distribution and electronic transitions. Table 11 presents the numerical analysis of the DOS spectrum, while Fig. 13 graphically represents the DOS distribution. The DOS spectrum of 3MPAEMA, as illustrated in Fig. 13, reveals key electronic properties by mapping the energy states for electrons at different energy levels.

3.7 Non-Covalent Interactions (NCI)

The study of non-covalent interactions (NCIs) in 3MPAEMA provides a deeper understanding of its

Table 4 The key FT-IR absorption bands observed in the spectrum of 3MPAEMA

Wavenumber (cm^{-1})	Intensity (%)	Functional Group Assignment
4000–3500	69–84	O-H stretching (broad), N-H stretching
3500–3000	73–84	C-H stretching (aromatic and aliphatic)
3000–2500	84–86	C-H stretching (methylene)
2500–2000	69–84	Combination and overtone bands
2000–1500	26–29	C = O stretching (carbonyl group)
1500–1000	10–20	C = C stretching, aromatic ring vibrations
1000–500	55–77	C-H bending, C-N stretching
500–0	73–86	Out-of-plane deformations, skeletal vibrations

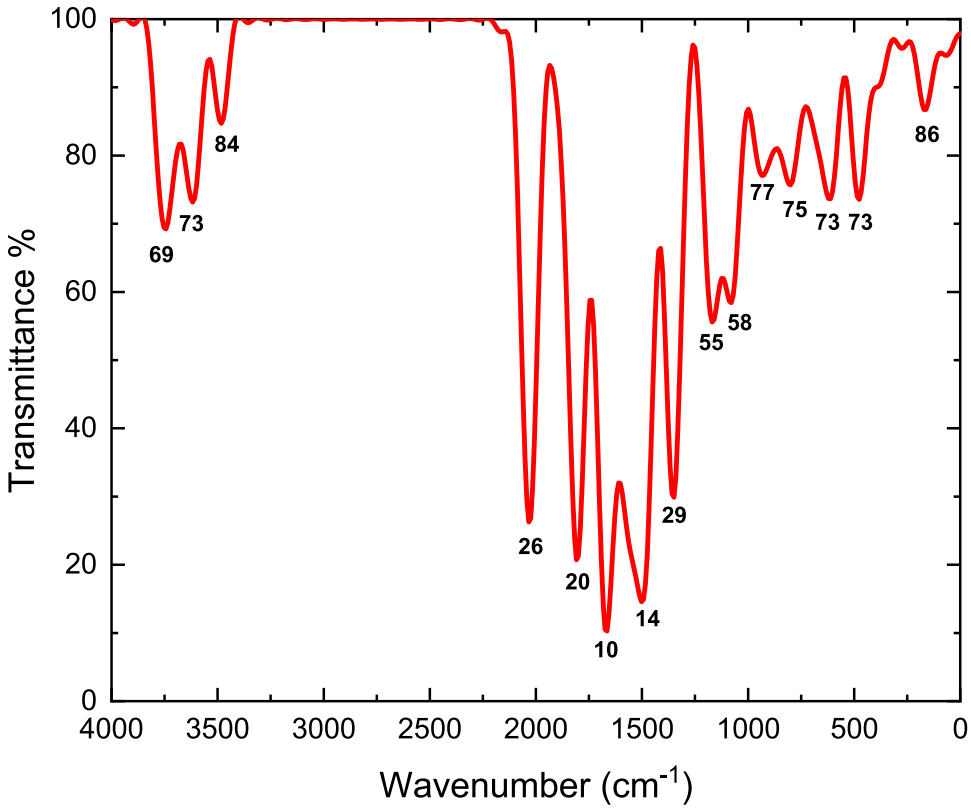

Fig. 6 Theoretical FT-IR spectrum of 3MPAEMA

Table 5 The theoretical ^{13}C NMR chemical shifts for 3MPAEMA

Carbon Atom	Chemical Shift (ppm)	Description and Assignment
C1	178.5	Carbonyl carbon of methacrylate group
C2	132.1	Methine carbon in methacrylate group
C3	61.4	Methylene carbon adjacent to oxygen
C4	48.7	Quaternary carbon attached to N and O groups
C5	155.8	Aromatic carbon attached to methoxy group
C6	120.3	Aromatic carbon in meta position to amino group
C7	113.6	Aromatic carbon para to methoxy group
C8	138.2	Aromatic carbon attached to amino group
C9	56.3	Methoxy group carbon attached to aromatic ring
C10	123.5	Aromatic carbon adjacent to amino group

Table 6 The theoretical ^{1}H NMR chemical shifts for 3MPAEMA

Proton	Chemical Shift (ppm)	Description and Assignment
H1	7.26	Aromatic proton attached to C5
H2	6.92	Aromatic proton in meta position to methoxy group
H3	6.82	Aromatic proton para to amino group
H4	5.45	Vinylic proton in methacrylate group
H5	3.78	Methoxy group proton
H6	2.32	Methylene protons adjacent to carbonyl
H7	1.80	Methyl group protons attached to C3
H8	1.23	Methyl group protons in aliphatic chain

intermolecular forces, stability, and potential reactivity. Using the Reduced Density Gradient (RDG) analysis, the interaction regions and their nature have been examined. The results from Table 12, and 13, Fig. 14, and 15 highlight key findings related to hydrogen bonding, van der Waals interactions, and steric effects. The RDG-based NCI visualization in Fig. 14 graphically represents the interaction regions within 3MPAEMA. The color-coded RDG surfaces indicate the presence and type of non-covalent interactions, which are crucial for determining molecular stability and reactivity.

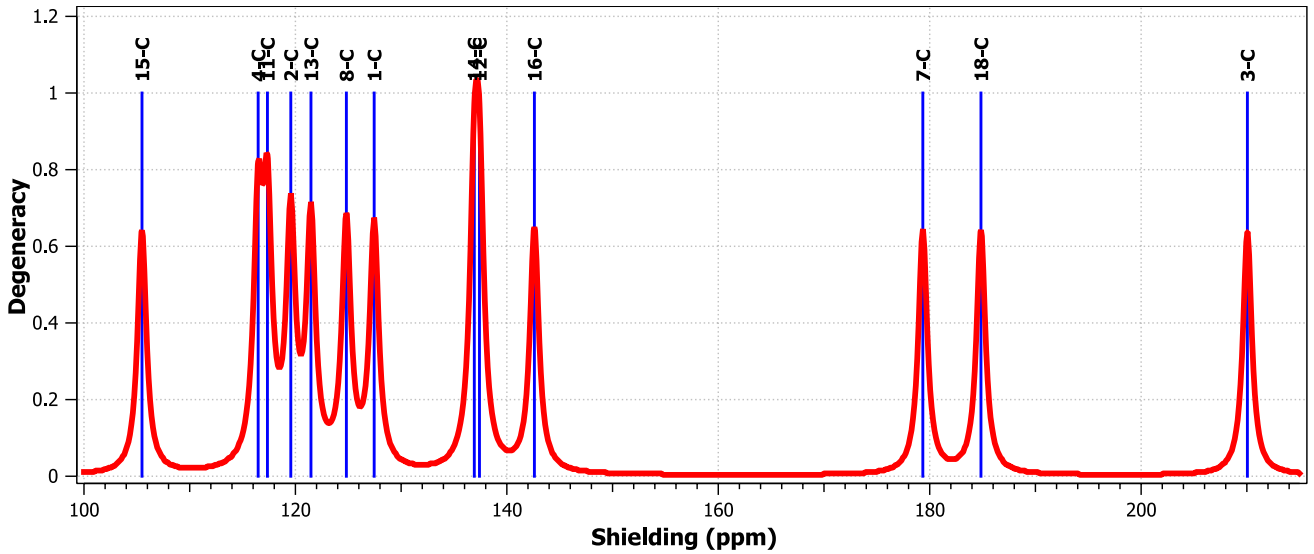

Fig. 7 Theoretical ^{13}C NMR spectra of 3MPAEMA

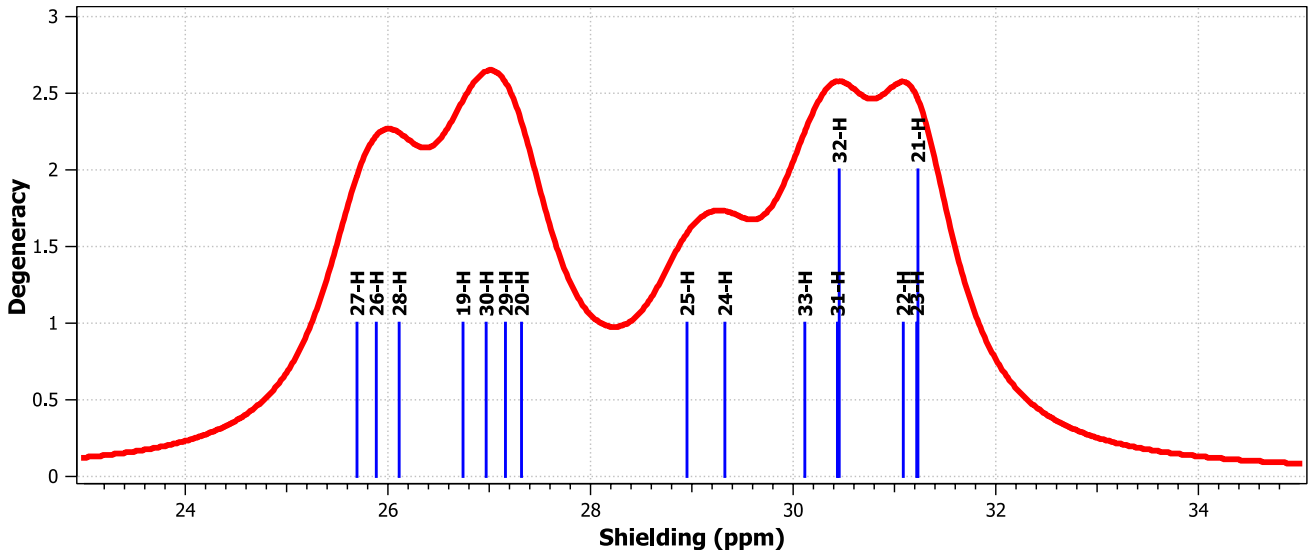

Fig. 8 Theoretical ^{1}H NMR spectra of 3MPAEMA

Table 7 The UV–Visible Spectroscopy for 3MPAEMA

N State	λmax (nm)	ε (M^{-1} cm^{-1})	Oscillator Strength (f)	Description
6	245	4000	0.040	Electronic transition in lower conjugation state
12	218	17500	0.175	Increased conjugation length and transition probability
24	198	27000	0.225	High-intensity transition with extended conjugation
64	185	25000	0.250	Broadening of absorption band with multiple transitions

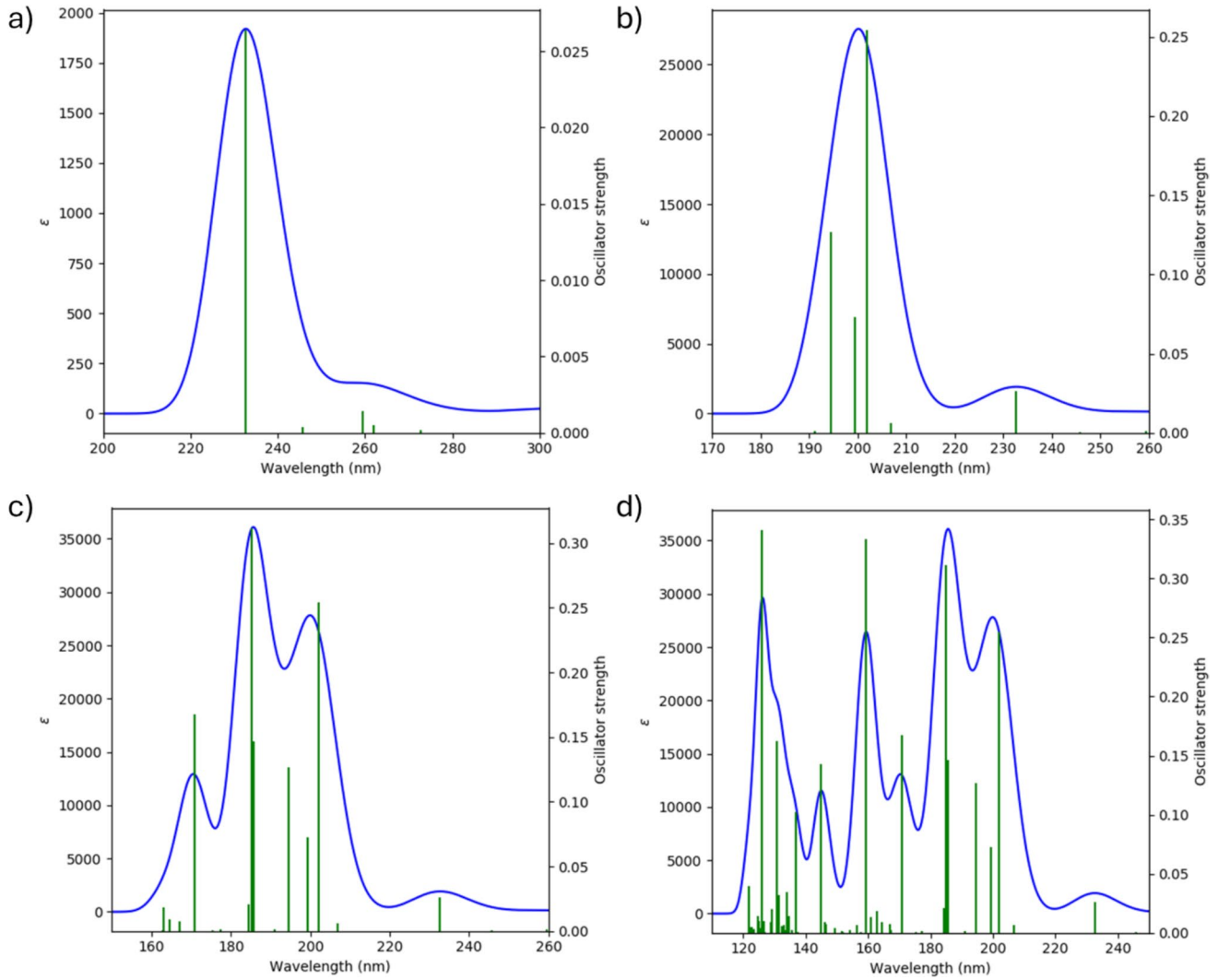

Fig. 9 UV–visible of N state **a**) 6 **b**) 12 **c**) 24 **d**) 64 absorptions of 3MPAEMA

Table 8 Analyzes the Molecular Electrostatic Potential (MEP) for the 3MPAEMA

Region	Electrostatic Potential	Associated Functional Groups	Implications for Reactivity and Interactions
Red (High Negative Potential)	Highly negative potential (indicated by red color)	Oxygen atoms (O5, O6, O9, O17) in methacrylate and methoxy groups	Likely sites for electrophilic attacks; potential hydrogen bonding sites with hydrogen bond donors
Blue (High Positive Potential)	Highly positive potential (indicated by blue color)	Hydrogen atoms bonded to electronegative atoms (e.g., N10)	Potential sites for nucleophilic attacks; likely to interact with negatively charged species or lone pairs
Green (Neutral Potential)	Relatively neutral potential (indicated by green color)	Aromatic ring (C11-C16) and other non-polar regions	Less reactive regions; low likelihood of participating in strong chemical interactions, serves as a stabilizing framework

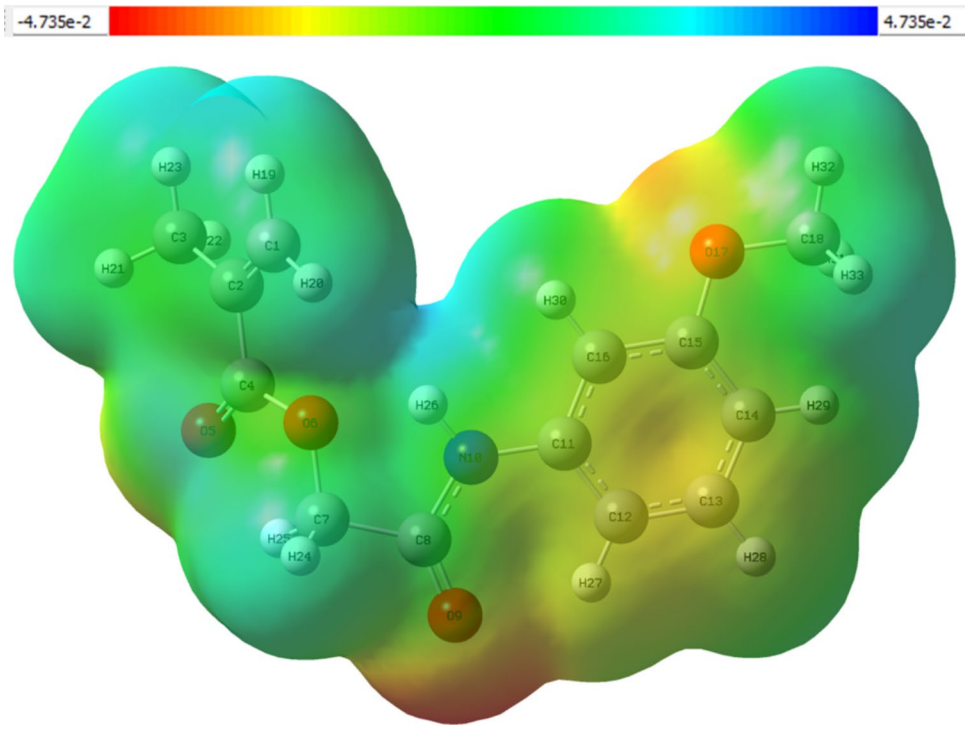

Fig. 10 Molecular electrostatic potential of 3MPAEMA

Table 9 A comprehensive analysis of the thermochemical properties of 3MPAEMA, including the interpretation of thermochemistry surface maps (TCSM) and the thermal behavior of E (thermal energy), CV (heat capacity), and S (entropy) across different temperature ranges

Parameter	Temperature Range (K)	Interpretation	Implications for Molecular Behavior
Thermochemistry Surface Maps (TCSM)	300–900	Visual representation of thermochemical energy distribution and potential energy surfaces	Red regions indicate high-energy areas, suggesting increased reactivity and thermodynamic activity. Blue and green regions are more stable with lower reactivity
Thermal Energy (E)	300–900	Increase in thermal energy with rising temperature	Indicates enhanced kinetic energy and more intense vibrational motion within the molecule
Heat Capacity (CV)	300–900	Variation in heat capacity as a function of temperature	Demonstrates the molecule's resistance to temperature changes and its ability to store thermal energy
Entropy (S)	300–900	Increase in entropy with temperature	Represents the increase in molecular disorder and randomness, affecting the spontaneity of reactions

3.8 Atomic and Molecular Electronic Properties

The ELF values range from 0 to 1, where higher values denote regions of significant electron localization, whereas lower values indicate electron delocalization or areas with minimal electron density [77]. The ELF data, summarized in Table 14 and visually represented in Fig. 16. High ELF values (0.8–1.0) are observed around oxygen atoms in carbonyl and ether groups, confirming localized electron density and strong lone-pair interactions. Moderate ELF values (0.5–0.7) are found in covalent bond regions, indicating well-defined bonding interactions within the molecular framework. Lower ELF values (< 0.3) are primarily localized in aliphatic and conjugated regions, suggesting delocalized electronic distributions, particularly in extended π-systems or flexible molecular domains. The ESP data, presented in Table 15 and illustrated in Fig. 17. Highly negative ESP regions (electron-rich, red areas) are concentrated around oxygen atoms, especially in carbonyl (-C = O) and ether (-O-) functional groups. These regions serve as potential nucleophilic attack sites for electrophiles. Moderately negative ESP regions are observed along polarized bonds, indicating areas where partial charge separation influences molecular interactions. Positive ESP regions (electron-deficient, blue areas) are found in hydrogen atoms attached to electronegative groups,

Table 10 Calculation of Parameters of E (Thermal), CV (heat capacity), S (entropy) of 3MPAEMA

Temperature (K)	Total			Translational			Rotational			Vibrational		
	E (Thermal) kcal/Mol	C_V (Cal/Mol-K)	S (Cal/Mol-K)	E (Thermal)	C_V (Cal/Mol-K)	S (Cal/Mol-K)	E (Thermal)	C_V (Cal/Mol-K)	S (Cal/Mol-K)	E (Thermal)	C_V (Cal/Mol-K)	S (Cal/Mol-K)
298	175.857	49.515	108.947	0.888	2.981	42.436	0.888	2.981	34.146	174.080	43.553	32.365
400	181.772	66.209	126.482	1.192	2.981	43.899	1.192	2.981	35.023	179.387	60.247	47.560
500	189.127	80.486	143.279	1.490	2.981	45.007	1.490	2.981	35.688	186.146	74.524	62.583
600	197.788	92.345	159.399	1.788	2.981	45.913	1.788	2.981	36.232	194.211	86.384	77.254
700	207.527	102.130	174.698	2.087	2.981	46.679	2.087	2.981	36.691	203.354	96.169	91.328
800	218.160	110.294	189.150	2.385	2.981	47.342	2.385	2.981	37.089	213.391	104.333	104.719
900	229.544	117.201	202.785	2.683	2.981	47.927	2.683	2.981	37.441	224.179	111.239	117.417
1000	241.567	123.108	215.656	2.981	2.981	48.451	2.981	2.981	37.755	235.605	117.146	129.451

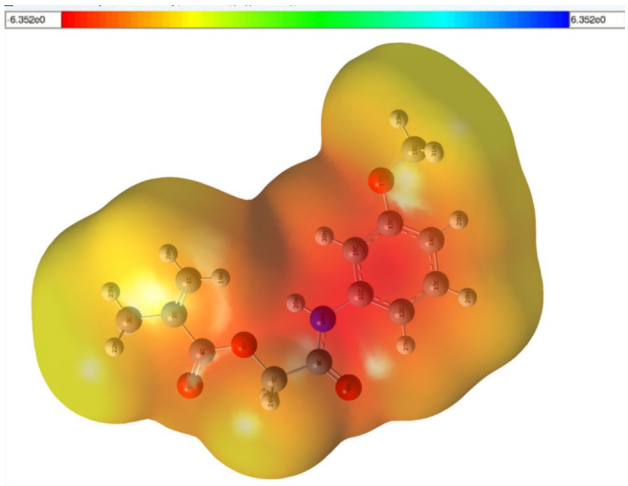

Fig. 11 Thermochemistry surface maps (TCSM) of 3MPAEMA

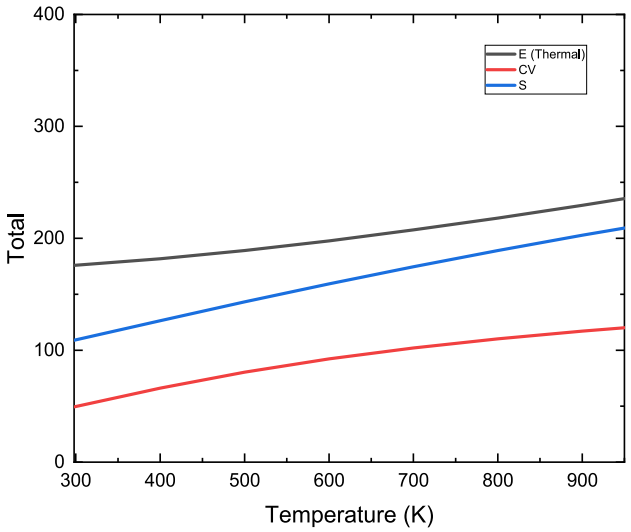

Fig. 12 Thermal investigation of E (thermal) energy, CV (heat capacity), and S (entropy) of 3MPAEMA

signifying their role as potential hydrogen-bond donors. The ALIE values, summarized in Table 16 and depicted in Fig. 18. High ALIE values are observed in oxygen-containing functional groups, particularly carbonyl and ether regions, suggesting that these sites require high energy for electron removal, reinforcing their chemical stability and low susceptibility to oxidation. Moderate ALIE values are present in C–C and C-H bonded regions, indicating balanced electronic stability across the molecular framework. Low ALIE values are observed in π-conjugated systems and flexible aliphatic chains, suggesting potentially weakly bound electrons that may facilitate electron transfer or interaction with electrophiles.

Table 11 A detailed analysis of the Density of States (DOS) spectrum of 3MPAEMA

Feature	Energy Range (eV)	Description	Implications for Molecular Behavior
DOS Spectrum (Blue Line)	−20 to + 10	Represents the density of electronic states available at each energy level	Peaks indicate highly populated energy levels; critical for understanding the electronic structure and stability of the molecule
Occupied Orbitals (Green Lines)	−20 to 0	Energy levels below the zero-energy level, occupied by electrons undergrounds-state conditions	Provides insights into bonding nature, electronic stability, and potential reactivity
Virtual Orbitals (Red Lines)	0 to + 10	Energy levels above the zero-energy level, representing unoccupied molecular orbitals	Indicates the potential for electronic transitions; smaller HOMO–LUMO gap suggests higher reactivity and electronic polarizability
HOMO–LUMO Gap	Defined by gap between highest occupied and lowest unoccupied orbitals	The energy gap between the highest occupied and lowest unoccupied molecular orbitals	Smaller gap indicates greater reactivity and lower stability, while a larger gap suggests lower reactivity and greater stability

3.9 Evaluation of Toxicity and Physical Properties

The Toxicity Estimation Software Tool (TEST), which leverages the QSAR methodology, has been widely adopted to quickly estimate the toxicological impacts of chemical substances. Using TEST in numerous research publications highlights its effectiveness, with substantial attention given to its underlying modeling and mathematical principles. As an open-source platform, it offers researchers a readily accessible repository of molecular data, supporting a broad range of scientific investigations [78]. According to the Fathead Minnow LC50 (96 h) results, the value calculated for the external test set is 0.83 -Log10(mol/L), representing the lethal concentration of the compound for Fathead minnow fish in the aquatic environment. A higher value indicates a lower toxicity, as a higher concentration is required for the organism to survive. In the training set, this value is calculated as 0.35 -Log10(mol/L), indicating that the model performs better on this data set, making the results more reliable. When examining the Daphnia Magna LC50 (48 h) values, the value for the external test set is calculated as 0.59 -Log10(mol/L), representing the lethal effect of the toxic compound on Daphnia magna over 48 h. In the training set, this value is determined to be 0.28 -Log10(mol/L), indicating that the model produces more accurate predictions with a lower error rate during training. For the Tetrahymena Pyriformis IGC50 (48 h) results, the value for the external test set it has been reported as 0.20 -Log10(mol/L), representing the inhibitory concentration on T. pyriformis. In the training set, the value has been calculated as 0.28 -Log10(mol/L), suggesting that the model performs better on external data. For the Oral Rat LD50, the values from the external test set are determined to be 0.03 -Log10(mol/kg), indicating the lethal dose in rats. The low error rate suggests that the model has successfully predicted on the external test set. In the training set, the value is 0.17 -Log10(mol/kg), implying less accuracy in predictions. The bioconcentration factor, calculated as 0.38 Log10 for the external test set, reflects the tendency of toxic substances to accumulate in Living organisms. In the training set, the value is 0.50 Log10, with a higher error rate observed. When evaluating the normal boiling point and other physical properties, the normal boiling point for the external test set is recorded as 19.91 °C, while in the training set, this value is observed as 25.56 °C. These differences suggest potential limitations in the model's ability to learn these physical properties. The melting point for the external test set is 46.33 °C, while in the training set, it is determined to be 77.83 °C. Regarding density, the value for the external test set is 0.05 g/cm^3, while in the training set, it is calculated as 0.01 g/cm^3, indicating that the model performs better on the training data. Surface tension and viscosity values reflect the molecular properties of the fluid, with the external test set having a surface tension

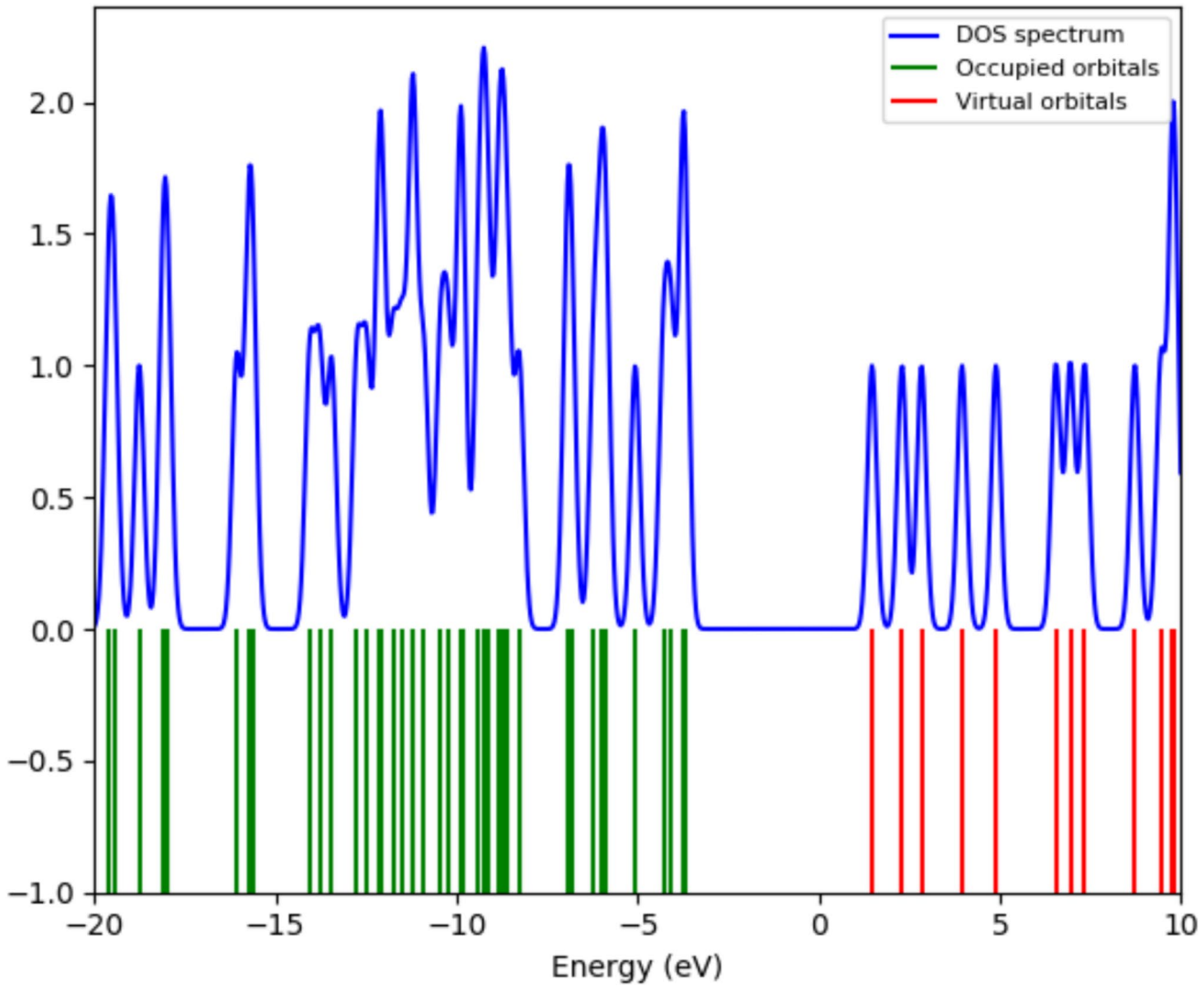

Fig. 13 Density of states (DOS) of 3MPAEMA

Table 12 A comprehensive analysis of different interaction regions for 3MPAEMA

Interaction Region	Color Indication	Type of Interaction	Implications for Molecular Behavior
Strong Attractive Interactions	Blue	Hydrogen bonds or other stabilizing non-covalent interactions	Indicates regions of strong attractive forces, contributing to the stability and potential binding sites of the molecule
Weak van der Waals Interactions	Green	Non-specific weak attractions between atoms or molecules	Represents regions of weak, non-directional interactions that contribute to overall molecular packing and weak binding
Steric Repulsions	Red	Destabilizing interactions due to close atomic proximity	Highlights areas of steric hindrance, which may affect the molecule's conformation and reactivity
Neutral Interactions	No specific color	Lack of significant attractive or repulsive interactions	Represents regions with minimal interaction, contributing little to the molecule's stability or reactivity

Table 13 A comprehensive analysis of the RDG vs. sign(λ2)ρ plot for 3MPAEMA

Region in Plot	Sign(λ2)ρ Range	Type of Interaction	Implications for Molecular Behavior
Blue and Green Regions	−0.05 to −0.01	Weak attractive interactions such as van der Waals forces	Indicates regions of weak non-covalent interactions, contributing to the overall stability and molecular packing without significantly affecting reactivity
Negative Red Regions	−0.01 to 0	Strong attractive interactions such as hydrogen bonds	Represents regions of strong attractive forces, playing a crucial role in stabilizing the molecular conformation and influencing binding properties
Positive Red Regions	0 to + 0.05	Repulsive interactions due to steric clashes or close atomic proximity	Indicates regions of steric hindrance, which may affect the molecular conformation, reactivity, and steric accessibility
Neutral Regions	Close to 0	Lack of significant non-covalent interactions	Represents regions where the electron density is relatively uniform, contributing little to the molecule's non-covalent interaction profile

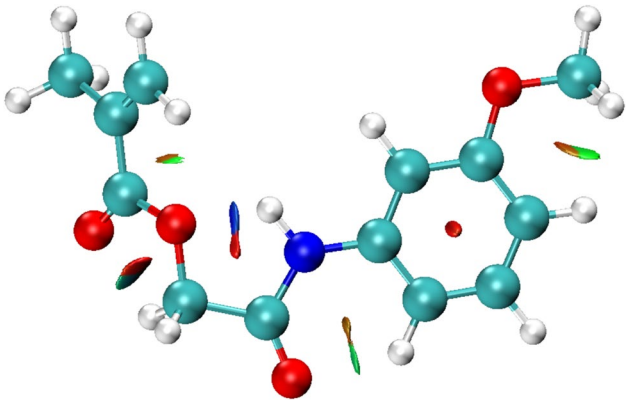

Fig. 14 Non-covalent interactions (NCI) analyses for 3MPAEMA

of 3.32 dyn/cm and the training set having a value of 0.18 dyn/cm. The viscosity for the external test set is recorded as 0.17 Log10(cP), while the training set has a value of 0.10 Log10(cP). The toxicities and physical properties of 3MPAEMA are presented in Table 17.

However, while the TEST platform facilitates rapid estimation of multiple endpoints, the results demonstrate a consistent disparity between training and test sets, suggesting potential overfitting in the QSAR models used. For several endpoints particularly physical properties such as melting point, boiling point, and surface tension model performance was notably better on the training set compared to the external test set. This gap raises concerns regarding model generalizability and reliability when applied to

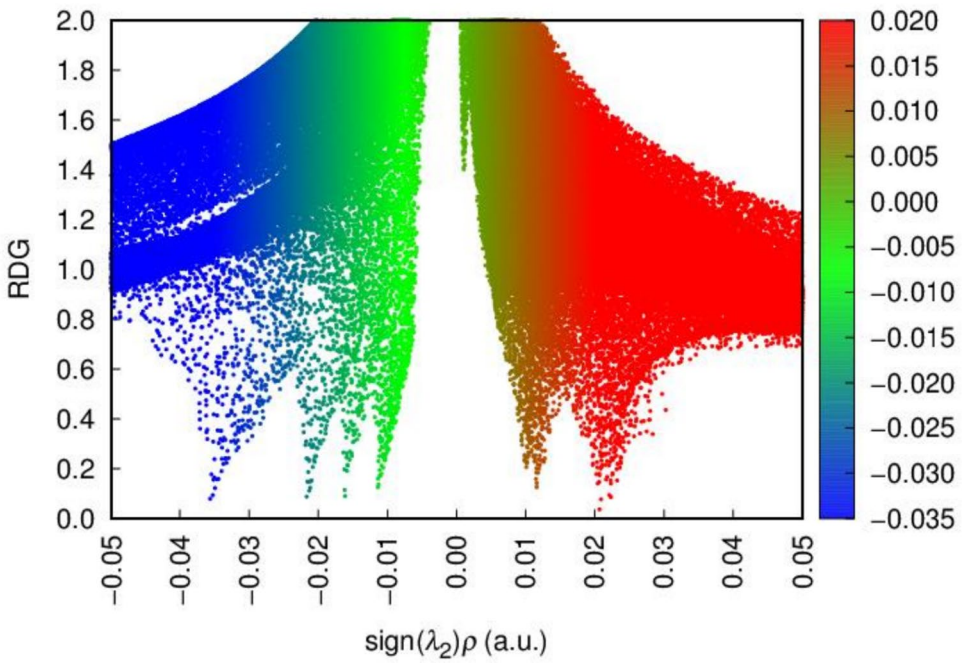

Fig. 15 Reduced density gradient (RDG) analyses for 3MPAEMA

Table 14 Electron Localization Function (ELF) Summary

Region	ELF Value Range	Type of Electron Localization	Implications for Molecular Behavior
High Localization (Red Regions)	0.9—1.0	Strong localization, corresponding to covalent bonds or lone pairs	Indicates areas with high electron density, suggesting strong covalent bonding or presence of lone pairs, contributing to molecular stability and specific reactivity sites
Moderate Localization (Green to Yellow Regions)	0.4—0.8	Moderate electron localization, often found in non-bonding regions	Represents regions of intermediate electron density, indicating weak interactions or regions with potential electronic flexibility
Low Localization (Blue Regions)	0.0—0.3	Delocalized electron density, such as in aromatic systems	Indicates regions with low electron localization, often associated with electron delocalization or metallic bonding, influencing the molecule's reactivity and aromatic character
Neutral Regions	Around 0.5	Uniform electron distribution, lack of significant localization	Represents regions with relatively uniform electron density, contributing little to chemical reactivity or specific interactions

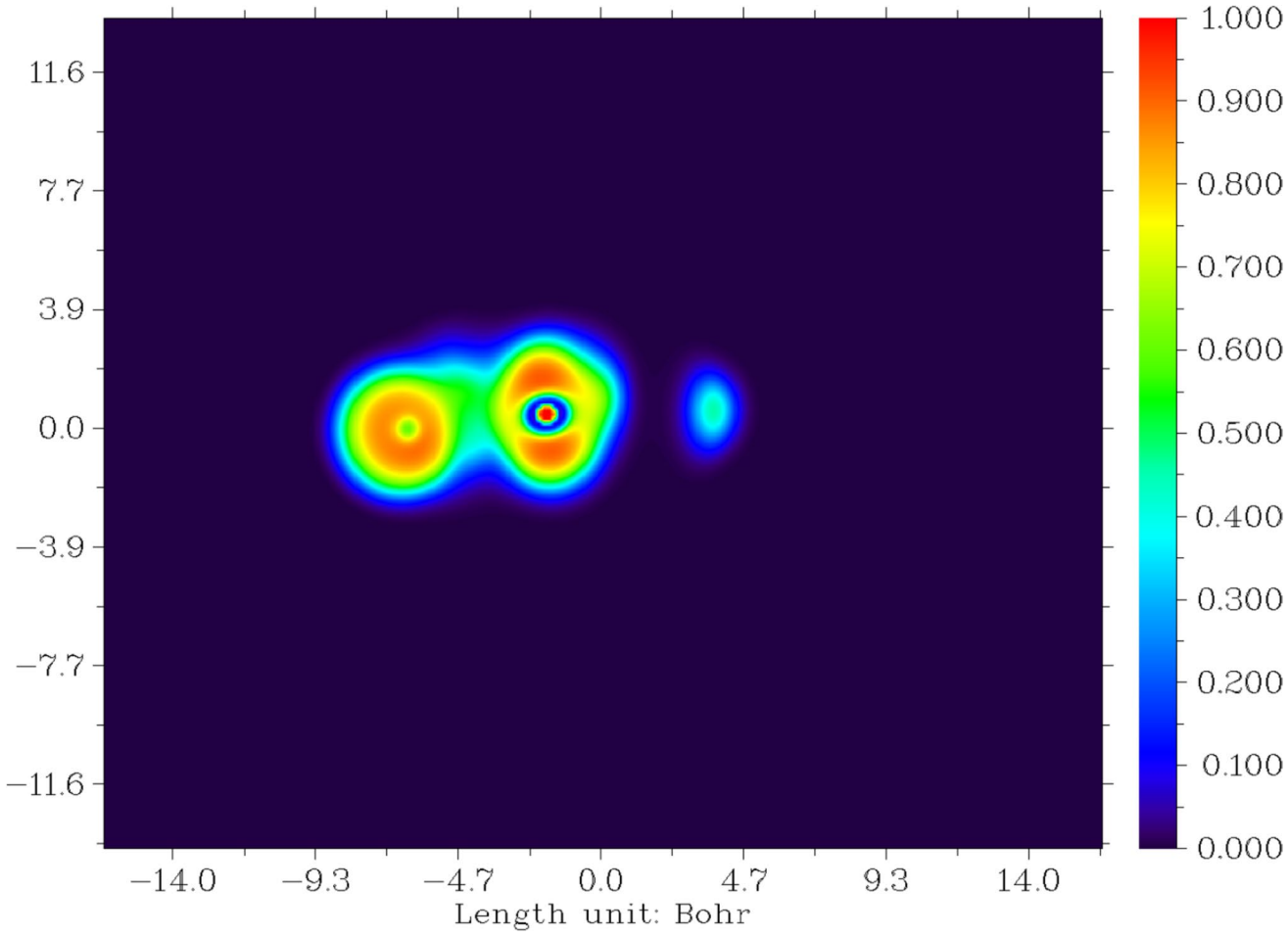

Fig. 16 Electron localization function (ELF) for 3MPAEMA

Table 15 Total electrostatic potential (ESP) summary

Region	ESP Value Range	Type of Electrostatic Interaction	Implications for Molecular Behavior
Positive Potential Regions (Red)	0.05 to 0.10	Electron-deficient areas, potential sites for nucleophilic attack	Indicates regions where nucleophiles might interact, suggesting potential reactivity sites for electrophilic substitution or binding interactions
Neutral Potential Regions (Green)	−0.02 to + 0.02	Balanced electron distribution, lack of significant charge	Represents regions with minimal reactivity, contributing little to specific chemical interactions but providing a stable environment
Negative Potential Regions (Blue)	−0.10 to −0.05	Electron-rich areas, potential sites for electrophilic attack	Indicates regions where electrophiles might interact, suggesting potential reactivity sites for nucleophilic substitution or hydrogen bonding
Transition Regions	−0.02 to + 0.05	Gradual change in electrostatic potential	Represents areas where the electrostatic potential transitions from negative to positive, indicating regions of potential dipole interactions and molecular polarity

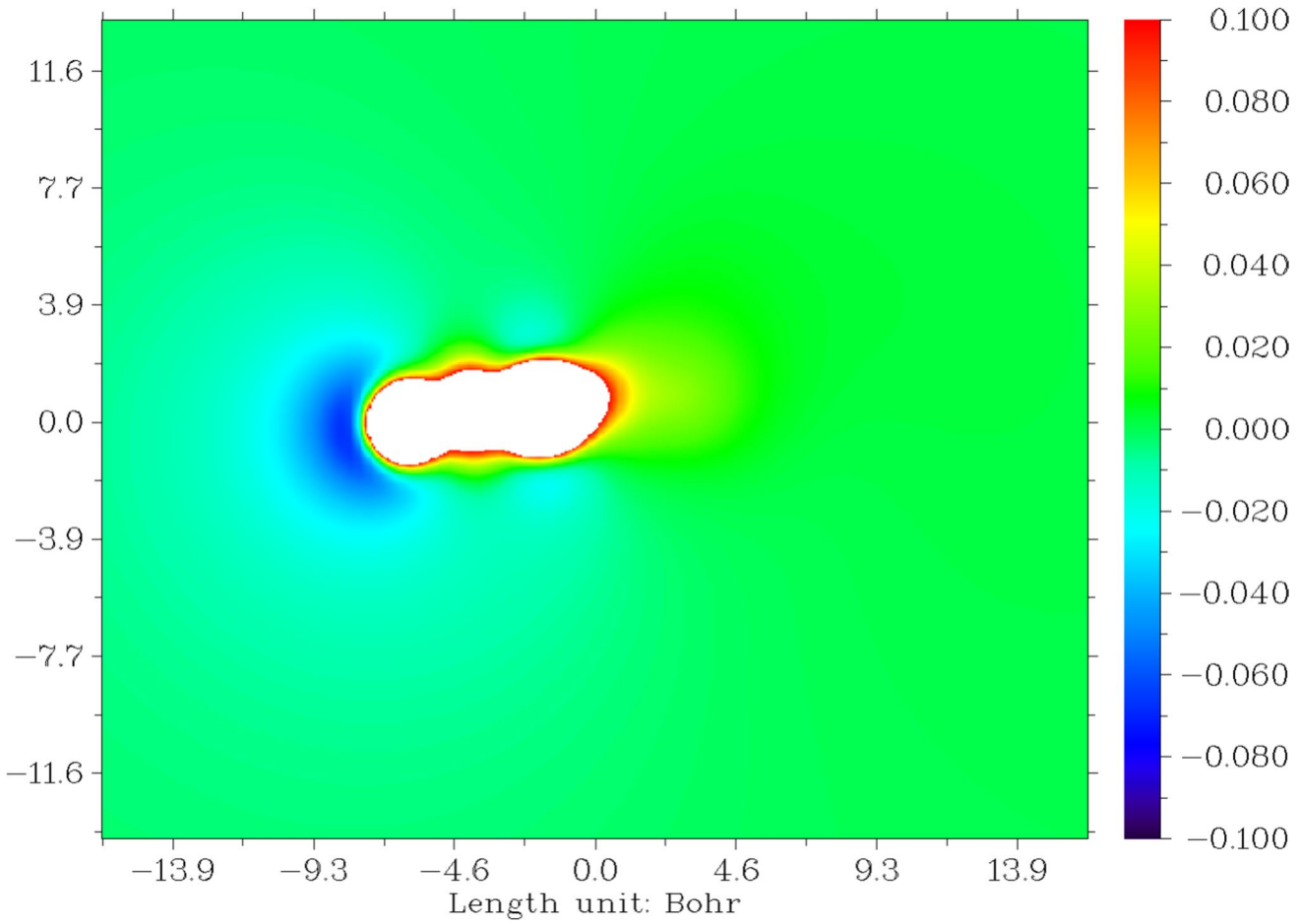

Fig. 17 Total electrostatic potential (ESP) for 3MPAEMA

Table 16 Average Local Ionization Energy (ALIE) Summary

Region	ALIE Value Range	Type of Ionization Energy	Implications for Molecular Behavior
High ALIE Regions (Red)	1.5–2.0	High ionization energy, tightly bound electrons	Indicates regions of high stability and low reactivity, suggesting areas less likely to participate in chemical reactions
Moderate ALIE Regions (Green to Yellow)	0.5–1.5	Moderate ionization energy, balanced electron binding	Represents regions with moderate stability, potentially involved in specific interactions but less reactive than low ALIE regions
Low ALIE Regions (Blue)	0.0–0.5	Low ionization energy, loosely bound electrons	Indicates regions of high reactivity, prone to electron removal and nucleophilic attack, suggesting potential sites for chemical reactions
Transition Regions	0.5–1.0	Gradual change in ionization energy	Represents areas where the ionization energy transitions, indicating regions with potential dipole interactions and moderate chemical activity

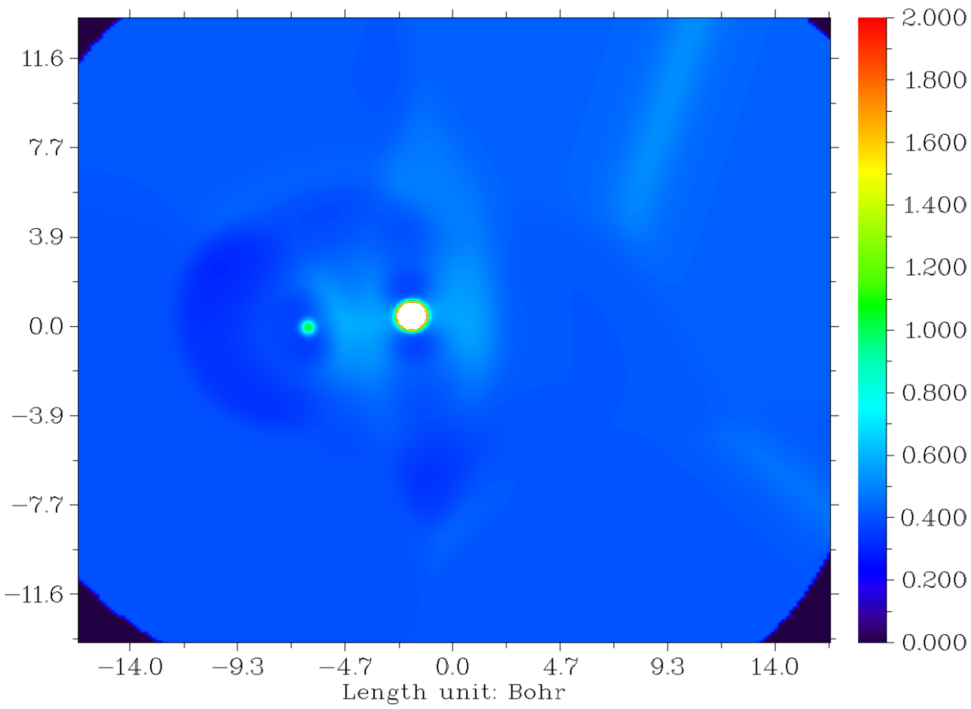

Fig. 18 Average local ionization energy (ALIE) for 3MPAEMA

novel compounds. Overfitting may occur when the model becomes too tailored to the training data, capturing noise rather than true predictive patterns. Therefore, while the low prediction error within the training set may indicate internal consistency, the reduced accuracy in external test predictions highlights the need for caution in interpretation. Future improvements may involve using larger and more diverse training datasets, applying rigorous validation techniques (e.g., cross-validation), and incorporating consensus modeling to mitigate overfitting and improve external predictive power. Acknowledging these limitations is essential for ensuring the credibility and applicability of QSAR-based toxicity assessments [79, 80].

3.9.1 Model Performance and Generalization in Toxicity Predictions

The Fathead Minnow LC50 (96 h) graphs depict the distribution of the lethal concentration of the toxic compound for Fathead minnow fish in both the external test and training sets. A broad and irregular distribution in the external test set indicates lower prediction accuracy of the model, whereas a narrower and more concentrated distribution in the training set suggests that the model learned these data better and has a higher capability to make accurate predictions. The Daphnia Magna LC50 (48 h) graphs represent the lethal concentrations encountered by the organism when exposed to

Table 17 Toxicities and physical properties of 3MPAEMA

Endpoint	MAE*	*Mean absolute error	Sets
Fathead minnow LC50 (96 h)	0.83	-Log10(mol/L)	external test set
	0.35		training set
Daphnia magna LC50 (48 h)	0.59	-Log10(mol/L)	external test set
	0.28		training set
T. pyriformis IGC50 (48 h)	0.20	-Log10(mol/L)	external test set
	0.28		training set
Oral rat LD50	0.03	-Log10(mol/kg)	external test set
	0.17		training set
Bioconcentration factor	0.38	Log10	external test set
	0.50		training set
Normal boiling point	19.91	°C	external test set
	25.56		training set
Vapor pressure at 25 °C	0.74	°C	external test set
	0.37		training set
Melting point	46.33	°C	external test set
	77.83		training set
Flash point	8.26	°C	external test set
	12.09		training set
Density	0.05	g/cm^3	external test set
	0.01		training set
Surface tension at 25 °C	3.32	dyn/cm	external test set
	0.18		training set
Viscosity at 25 °C	0.17	Log10(cP)	external test set
	0.10		training set
Water solubility at 25 °C	0.28	Log10(mol/L)	external test set
	0.53		training set

the toxic compound. Differences between the distributions in the external test set and the training set provide insights into the model's performance and its ability to generalize to external data. In the Tetrahymena Pyriformis IGC50 (48 h) graphs, more scattered data points in the external test set suggests lower model performance on external data, whereas the dense and focused data distribution in the training set indicates increased prediction accuracy for this organism. The Oral Rat LD50 graphs allow for the observation of how the lethal doses of the toxic substance change across the external test and training sets. A more concentrated data distribution in the training set signifies better model performance on this data. Bioconcentration factor graphs visualize the tendency of toxic substances to accumulate within living organisms. Similarities between the training and external test sets indicate the model's success in learning these factors and its generalization capability. When comparing the model's performance across different physical and chemical properties in both the external test and training sets, limitations in the model's ability to adapt to external data were observed in some properties. This suggests that the model may require additional training data to improve its generalization capabilities.

3.9.2 Oral Toxicity Prediction and Molecular Docking Analyses

According to the data obtained with ProTox 3.0 and given in Table 18, both compounds exhibit significant activity on respiratory and neurological pathways, indicating the potential for systemic effects. Organ toxicity parameters such as hepatotoxicity and neurotoxicity have been classified as"inactive"(with probabilities of 60% and 58%, respectively). This suggests that the compound does not exhibit significant toxic effects on the liver and nervous system. Nephrotoxicity and respiratory toxicity have been predicted as active (with probabilities of 70% and 52%, respectively). This indicates that the compound may have potential toxic effects on the kidneys and respiratory system. Cardiotoxicity is classified as inactive (with a probability of 67%), indicating a low risk of significant toxic effects on the heart. Carcinogenicity, immunotoxicity, mutagenicity, and cytotoxicity have been evaluated as inactive. The probability of immunotoxicity being inactive is high (87%). The blood–brain barrier (BBB) and clinical toxicity have been classified as active (with probabilities of 60% and 61%, respectively). This suggests that the compound may have systemic and

Table 18 Results for similar chemicals

Classification	Target	Prediction	Probability
Organ toxicity	Hepatotoxicity	Inactive	0.60
Organ toxicity	Neurotoxicity	Inactive	0.58
Organ toxicity	Nephrotoxicity	Active	0.70
Organ toxicity	Respiratory toxicity	Active	0.52
Organ toxicity	Cardiotoxicity	Inactive	0.67
Toxicity end points	Carcinogenicity	Inactive	0.64
Toxicity end points	Immunotoxicity	Inactive	0.87
Toxicity end points	Mutagenicity	Inactive	0.62
Toxicity end points	Cytotoxicity	Inactive	0.63
Toxicity end points	BBB-barrier	Active	0.60
Toxicity end points	Ecotoxicity	Inactive	0.67
Toxicity end points	Clinical toxicity	Active	0.61
Toxicity end points	Nutritional toxicity	Inactive	0.61
Tox21-Nuclear receptor signaling pathways	Aryl hydrocarbon Receptor (AhR)	Inactive	0.66
Tox21-Nuclear receptor signaling pathways	Androgen Receptor (AR)	Inactive	0.98
Tox21-Nuclear receptor signaling pathways	Androgen Receptor Ligand Binding Domain (AR-LBD)	Inactive	0.97
Tox21-Nuclear receptor signaling pathways	Aromatase	Inactive	0.93
Tox21-Nuclear receptor signaling pathways	Estrogen Receptor Alpha (ER)	Inactive	0.83
Tox21-Nuclear receptor signaling pathways	Estrogen Receptor Ligand Binding Domain (ER-LBD)	Inactive	0.96
Tox21-Nuclear receptor signaling pathways	Peroxisome Proliferator Activated Receptor Gamma (PPAR-Gamma)	Inactive	0.91
Tox21-Stress response pathways	Nuclear factor (erythroid-derived 2)-like 2/antioxidant responsive element (nrf2/ARE)	Inactive	0.73
Tox21-Stress response pathways	Heat shock factor response element (HSE)	Inactive	0.73
Tox21-Stress response pathways	Mitochondrial Membrane Potential (MMP)	Inactive	0.87
Tox21-Stress response pathways	Phosphoprotein (Tumor Suppressor) p53	Inactive	0.78
Tox21-Stress response pathways	ATPase family AAA domain-containing protein 5 (ATAD5)	Inactive	0.93
Molecular Initiating Events	Thyroid hormone receptor alpha (THRα)	Inactive	0.57
Molecular Initiating Events	Thyroid hormone receptor beta (THRβ)	Inactive	0.67
Molecular Initiating Events	Transtyretrin (TTR)	Inactive	0.74
Molecular Initiating Events	Ryanodine receptor (RYR)	Inactive	0.91
Molecular Initiating Events	GABA receptor (GABAR)	Inactive	0.69
Molecular Initiating Events	Glutamate N-methyl-D-aspartate receptor (NMDAR)	Inactive	0.97
Molecular Initiating Events	alpha-amino-3-hydroxy-5-methyl-4-isoxazolepropionate receptor (AMPAR)	Inactive	1
Molecular Initiating Events	Kainate receptor (KAR)	Inactive	0.99
Molecular Initiating Events	Achetylcholinesterase (AChE)	Inactive	0.84
Molecular Initiating Events	Constitutive androstane receptor (CAR)	Inactive	0.99
Molecular Initiating Events	Pregnane X receptor (PXR)	Inactive	0.68
Molecular Initiating Events	NADH-quinone oxidoreductase (NADHOX)	Inactive	0.69
Molecular Initiating Events	Voltage gated sodium channel (VGSC)	Inactive	0.65
Molecular Initiating Events	Na+/I- symporter (NIS)	Inactive	0.72
Metabolism	Cytochrome CYP1A2	Inactive	0.73
Metabolism	Cytochrome CYP2C19	Inactive	0.76
Metabolism	Cytochrome CYP2C9	Inactive	0.59
Metabolism	Cytochrome CYP2D6	Inactive	0.80
Metabolism	Cytochrome CYP3A4	Active	0.54
Metabolism	Cytochrome CYP2E1	Inactive	0.99

neurological effects. Ecotoxicity and nutritional toxicity have been predicted as inactive. Targets such as Aryl Hydrocarbon Receptor (AhR) and Androgen Receptor (AR) have been classified as"inactive"supported by high confidence levels (83–98%). Other targets such as estrogen receptors (ER and ER-LBD) and PPAR-gamma have also been evaluated as inactive. Nrf2/ARE, HSE, and other stress response pathways have been classified as inactive. Specifically, predictions for MMP and ATAD5 are supported by high probabilities (87% and 93%, respectively). This indicates a low potential for the compound to trigger cellular stress responses. All molecular targets, such as thyroid hormone receptors (THRα and THRβ), GABA receptor (GABAR), and voltage-gated sodium channel (VGSC), have been classified as inactive. This suggests that the compound does not significantly interact with these receptors. Most cytochrome P450 enzymes (e.g., CYP1A2, CYP2D6) have been classified as inactive. However, CYP3A4 is predicted to be active (with a probability of 54%). This may indicate that the compound could be metabolized by this enzyme. In the study, the interaction of 3MPAEMA with target proteins identified through protox analysis was also investigated using molecular docking analysis. According to the results obtained, the binding energy for the CYP3A4 proteins was greater than −7 kcal/mol. The CYP3A4 protein, which is responsible for the biotransformation of drugs/chemicals, was identified as"active"in the protox analysis. Consistent with the protox analysis, the binding energy determined in the molecular docking analysis was −7.1 kcal/mol. Cytochrome P450 3A4 (CYP3A4) is the primary enzyme responsible for the oxidative metabolism of numerous drugs. Inhibiting this enzyme often results in the unwanted buildup of the administered therapeutic compound [78]. It is not known which CYP enzyme biotransforms the studied molecules. They may also be metabolized by the CYP1A1 enzyme. Experimental studies are needed to clarify this situation. The interaction of 3MPAEMA with Human toxicity proteins provides crucial insights into its biocompatibility, potential toxicity, and binding specificity. The binding position and the number of hydrogen bonds formed between 3MPAEMA and various human toxicity proteins are analyzed using Fig. 19, which illustrate different binding configurations. The two-dimensional (2D) and three-dimensional (3D) molecular structures were generated using ChemDraw Ultra 8.0 and GaussView 6.0. To construct reliable 2D-QSAR models and assess the relationship between structural features and inhibitory activity, a wide range of molecular descriptors were calculated for each compound in the dataset using three computational tools [81]. Such computational analyses guide the rational design of more potent and selective next-generation molecules [82]. The compounds detailed in reference were employed as an external test set to gauge the robustness and predictive power of the 3D-QSAR models [83].

For molecular docking analysis, human toxicity proteins were selected, and their corresponding PDB codes are listed in the Table 19.

3.10 Molecular Docking and Dynamic Analyses with STAT3 Protein

The three-dimensional structures of the proteins were obtained in PDB file format from the RCSB PDB protein database (https://www.rcsb.org/). Molecular docking calculations were conducted using AutoDock, and the interactions, including hydrogen (H)-bonds, were visualized using the Seamdock online tool. Molecular dynamics analyses of the protein and protein–ligand complexes were carried out using WebGro. The stability of the protein in both unbound and ligand-bound states was graphically depicted using RMSD plots. The binding energies of 3MPAEMA to *Homo sapiens* protein STAT3 (PDB ID: 6NJS) protein were calculated using the Autodock Vina, Seamdock programs. The 3D structure of STAT3 is given in Fig. 20. The binding energies of 3MPAEMA to STAT3 proteins are shown in Table 20, Fig. 21.

To validate the docking method, 3MPAEMA-STAT3 was placed at the binding site and analyzed with both Autodock and Seamdock. The Autodock analysis yielded a value of 6.9 kcal/mol, while the Seamdock analysis yielded a value of 6.8 kcal/mol. The molecular dynamics studies analyzed the structure of the STAT3 protein and its complex with 3MPAEMA. Figure 22 illustrates these analyses, focusing on the STAT3 protein alone and its interaction with 3MPAEMA. The RMSD values of the protein–ligand complexes during the 50 ns molecular dynamics simulations exhibited stability, oscillating between 0.3 and 0.4 nm (3.0–4.0 Å), signifying that the complexes maintained their structural integrity throughout the simulation (Fig. 22 and 23). RMSD graphs, which measure the stability of a complex structure over time, reveal that the RMSD value for the STAT3 protein remains steady at 0.25 nm. Meanwhile, the stability of the STAT3-3MPAEMA complex stabilizes at 0.5 nm and is maintained 50 ns. In the hydrogen bond analysis, an increase in the number of bonds correlates with a reduction in the energy levels of pharmacological systems. The findings suggest that the average energies of the STAT3-3MPAEMA complex are higher than those of the STAT3 protein alone, indicating a more effective solubilization effect for the STAT3-3MPAEMA combination compared to other compounds. Figure 21 and Table 20 summarizes the molecular dynamics study, presenting the stability of binding energies for the STAT3 protein and its complex with 3MPAEMA. Figure 23 shows the molecular dynamics study showing the stabilities of the binding energies of STAT3 protein and STAT3-3MPAEMA combinations.

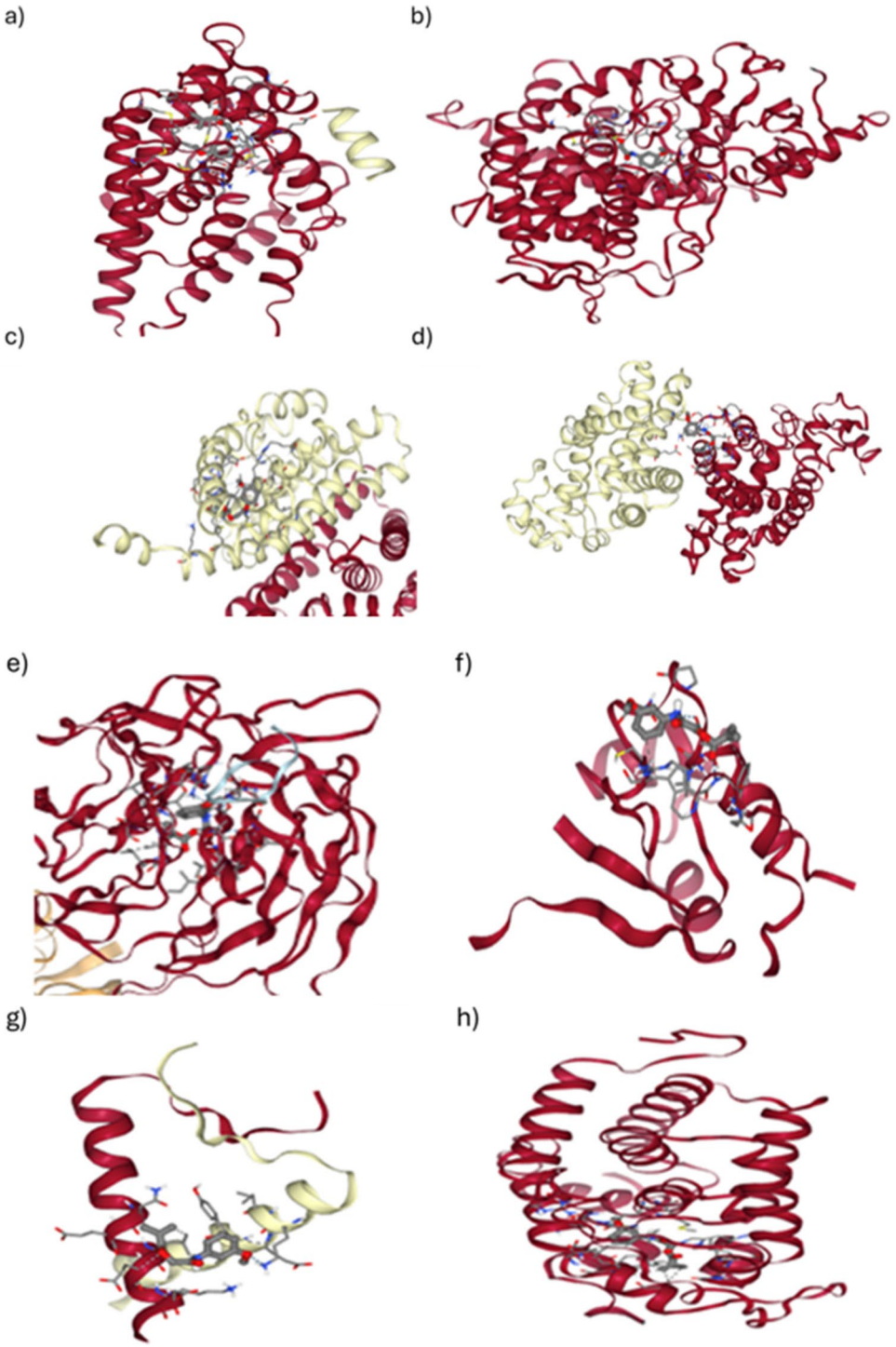

Fig. 19 Binding configurations of 3MPAEMA with human toxicity (a-t demonstrate the interactions of 3-MPAEMA with human toxicity-associated proteins, respectively)

In the in silico docking and dynamic analysis, 3MPAEMA showed favorable binding affinity toward STAT3, with key interactions observed at the SH2 domain, which is crucial for STAT3 dimerization and activation. The binding energy and interaction profiles suggest that 3MPAEMA may act as a potential STAT3 inhibitor. These findings indicate that 3MPAEMA could interfere with STAT3 signaling, which is upregulated in various cancer types. STAT3 is a well-established oncogenic transcription factor involved in tumor proliferation, survival, immune evasion, and angiogenesis [84, 85]. Its persistent activation has been observed in many human malignancies. Therefore, targeting STAT3 offers significant therapeutic potential. Our study supports this by suggesting that 3MPAEMA might contribute to STAT3 inhibition, opening avenues for further development as an anticancer agent.

Fig. 19 (continued)

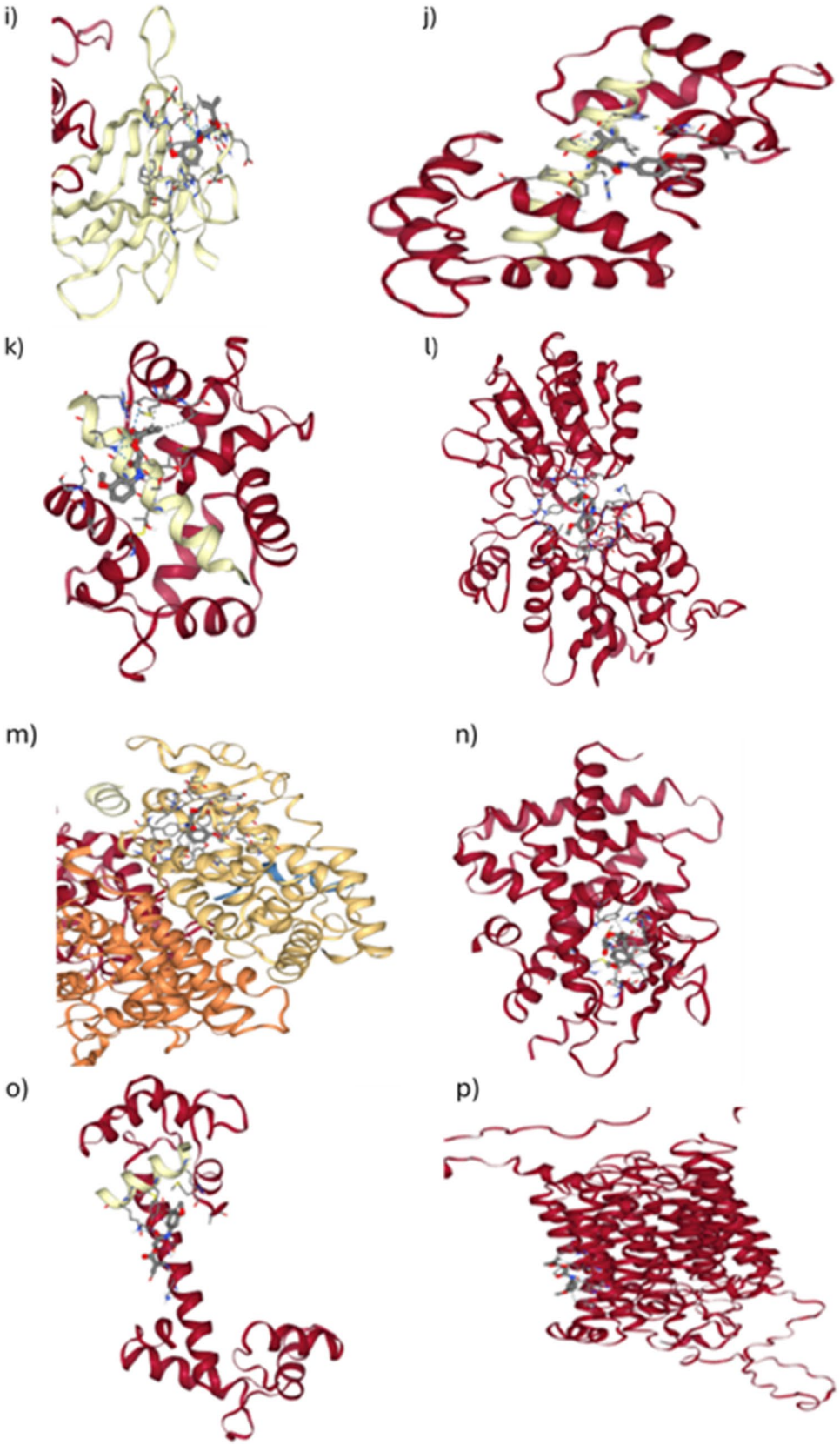

Fig. 19 (continued)

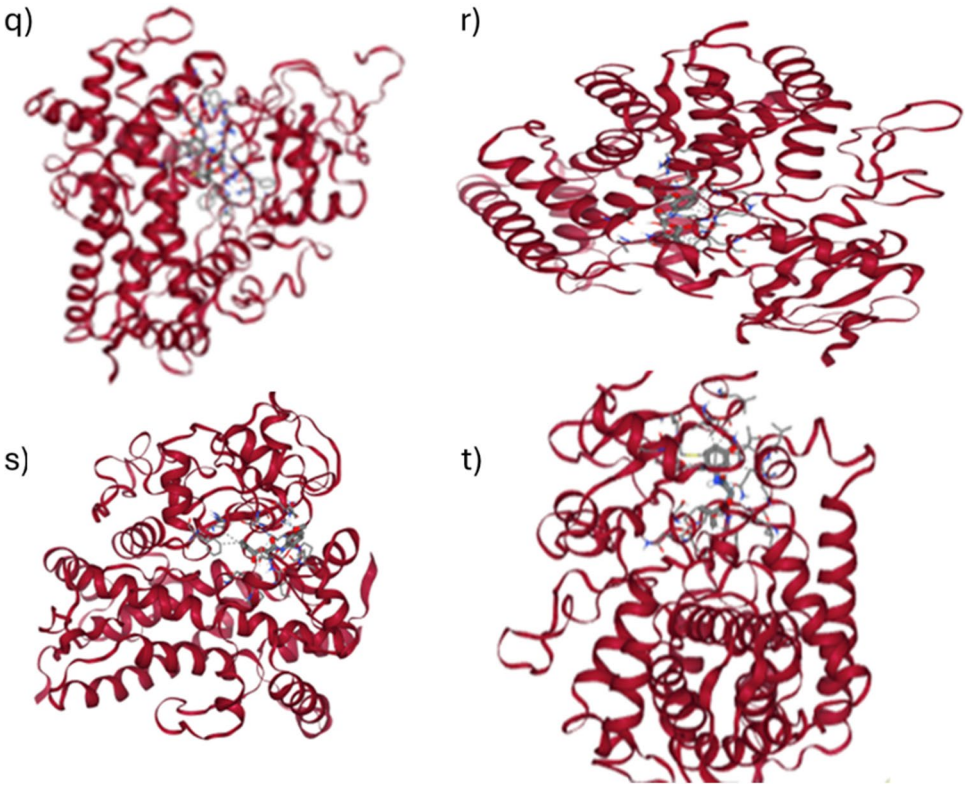

Table 19 Binding position and number of hydrogen bonds of 3MPAEMA to human toxicity proteins

Proteins and PDB ID code	Binding energy (kcal/mol)	Hydrogen Bound number
Androgen Receptor (AR) (PDB ID: 1T5Z)	-6.8	5
Aromatase (PDB ID: 3S79)	-6.5	3
Estrogen Receptor Alpha (ER) (PDB ID: 1A52)	-6.9	2
Peroxisome Proliferator Activated Receptor Gamma (PPAR-Gamma)(PDB ID: 1I7I)	-5.5	3
Nuclear factor (erythroid-derived 2)-like 2/antioxidant responsive element (nrf2/ARE) (PDB ID: 5WFV)	-6.8	4
Heat shock factor response element (HSE) (PDB ID: 5HDG)	-4.8	4
Mitochondrial Membrane Potential (MMP) (PDB ID: 1A1U)	-4.8	1
Thyroid hormone receptor alpha (THRα) (PDB ID: 2h77)	-6.8	2
Transtyretrin (TTR) (PDB ID: 1BZ8)	-5.7	5
Ryanodine receptor (RYR) (PDB ID: 6Y4P)	-5.3	3
GABA receptor (GABAR) (PDB ID: 3BYA)	-6.1	9
alpha-amino-3-hydroxy-5-methyl-4-isoxazolepropionate receptor (AMPAR) (PDB ID: 2WJW)	-6.3	6
Constitutive androstane receptor (CAR) (PDB ID: 1XVP)	-6.8	0
Pregnane X receptor (PXR) (PDB ID: 1ILG)	-6.7	0
Voltage gated sodium channel (VGSC) (PDB ID: 4DJC)	-5.4	5
Na+/I- symporter (NIS) (AlphaFold*: AF-Q92911-F1 *(https://www.alphafold.ebi.ac.uk/)	-5.4	1
Cytochrome CYP1A2 (PDB ID: 2HI4)	-6.1	1
Cytochrome CYP2C9 (PDB ID: 5A5I)	-6.5	1
Cytochrome CYP3A4 (PDB ID: 1TQN)	-7.1	3
Cytochrome CYP2E1 (PDB ID: 3E4E)	-6.7	3

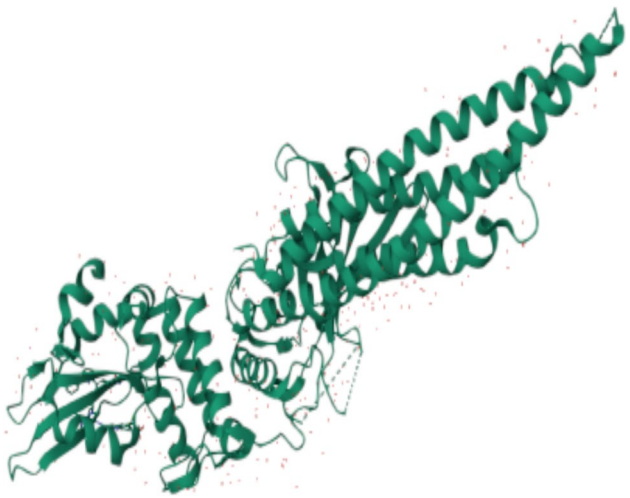

Fig. 20 3D structure of STAT3 (https://www.rcsb.org/3d-view/6NJS/1)

Table 20 Binding position and number of hydrogen bonds of 3MPAEMA to STAT3 protein

STAT3 (6NJS)	Binding energy (kcal/mol)	Hydrogen Bound number	Binding position
3MPAEMA	−6,9	10	Figure 21

Root Mean Square Fluctuation (RMSF) analysis was performed to evaluate the flexibility of each residue during molecular dynamics simulations for the apo form of the protein and the ligand-bound complex [86, 87]. RMSF values provide insight into residue-specific mobility and may reflect conformational changes upon ligand binding. As shown in Fig. 24 apo protein and protein–ligand complex, both systems exhibit generally low to moderate fluctuations in most regions of the protein, especially in the structured core domains (approximately 50–300 residues). However, notable differences were observed, especially in the terminal regions. In the apo form, a significant increase in fluctuation was detected in the C-terminal region, indicating substantial flexibility, with RMSF values reaching up to ~ 0.9 nm. The corresponding region in the protein–ligand complex showed a markedly reduced fluctuation, with RMSF values peaking at approximately 0.5 nm. This decrease suggests that ligand binding provides additional stability to the C-terminal residues, possibly through direct or allosteric interactions that restrict the conformational freedom of this segment.

An overall decrease in RMSF values was observed in several other regions of the protein upon ligand binding, indicating a global stabilizing effect induced by the ligand. This suggests that ligand interaction may promote a more compact and stable conformation, potentially increasing functional or structural integrity. These

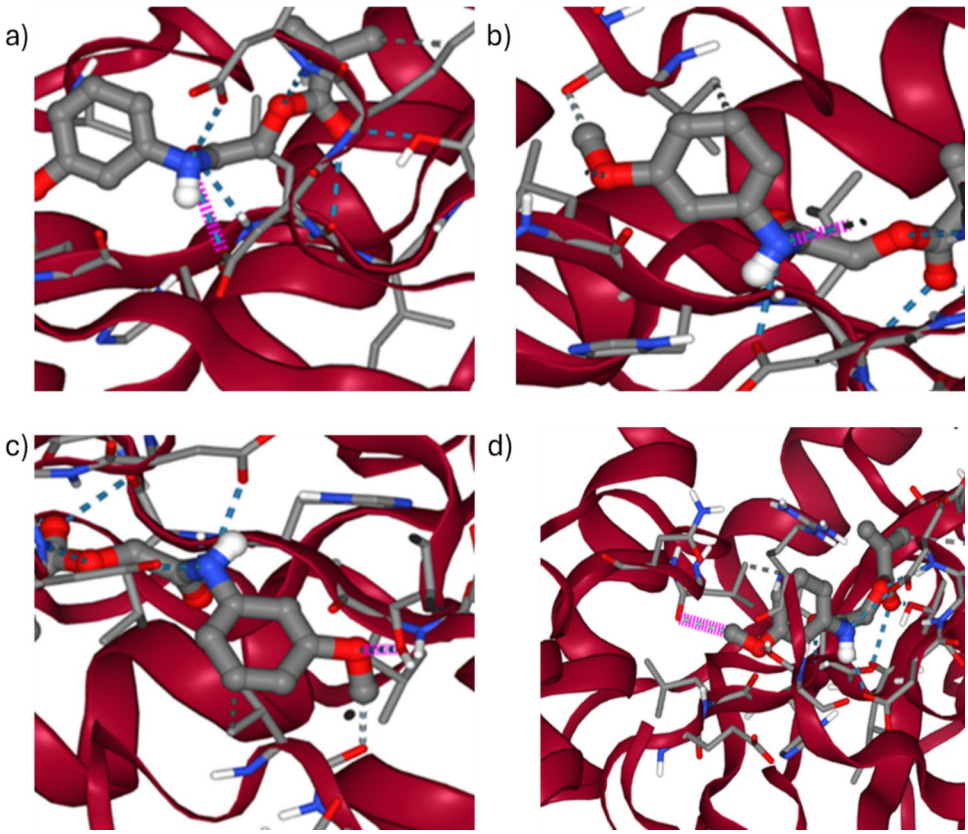

Fig. 21 **a-d.** Binding position of 3MPAEMA to STAT3 protein

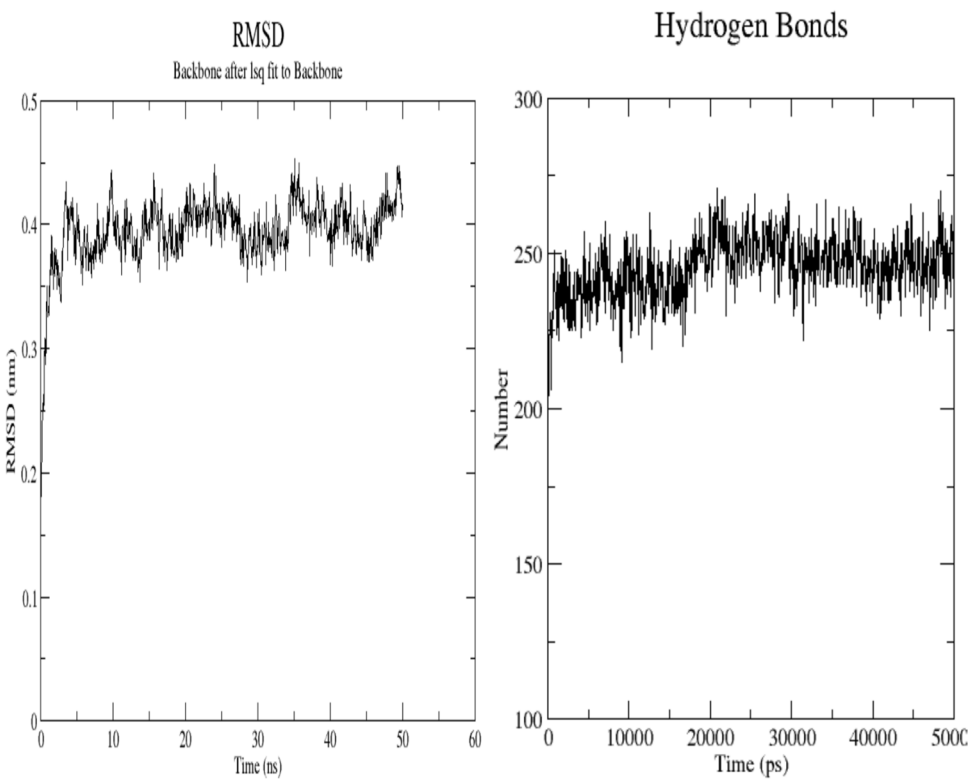

Fig. 22 RMSD and Hydrogen bounds graphs of STAT3 proteins

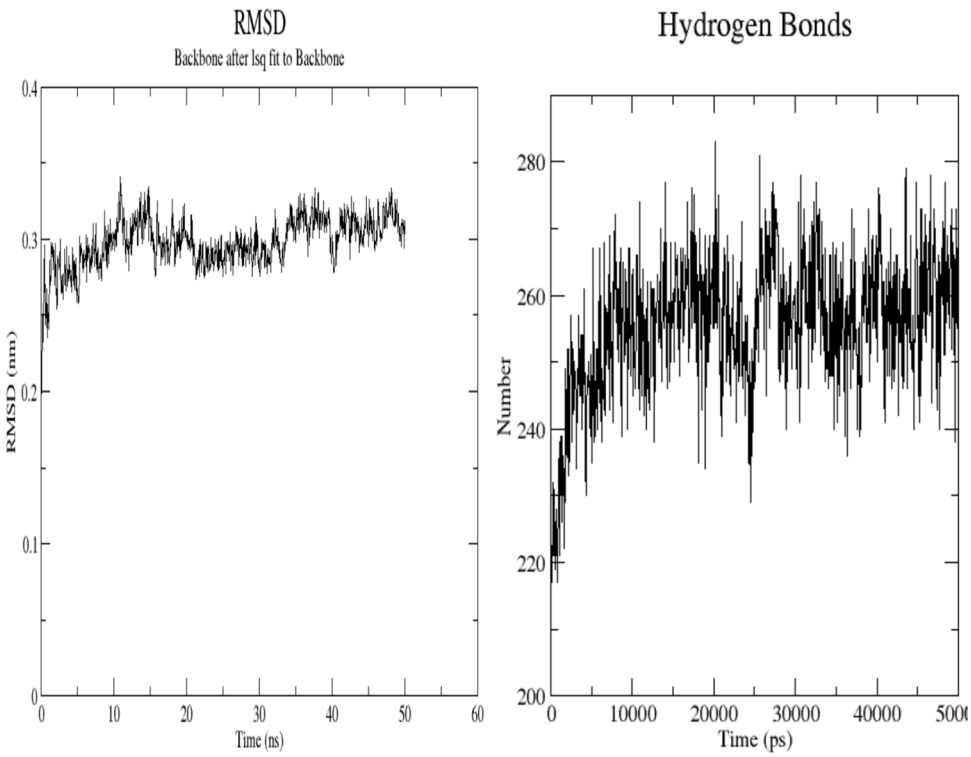

Fig. 23 RMSD and Hydrogen bounds graphs of STAT3-3MPAEMA complex

findings suggest that ligand binding significantly regulates the dynamic behavior of the protein, primarily by reducing the flexibility of key regions. This stabilization may be crucial for the proper functioning and structural maintenance of the protein in its active or ligand-bound state.

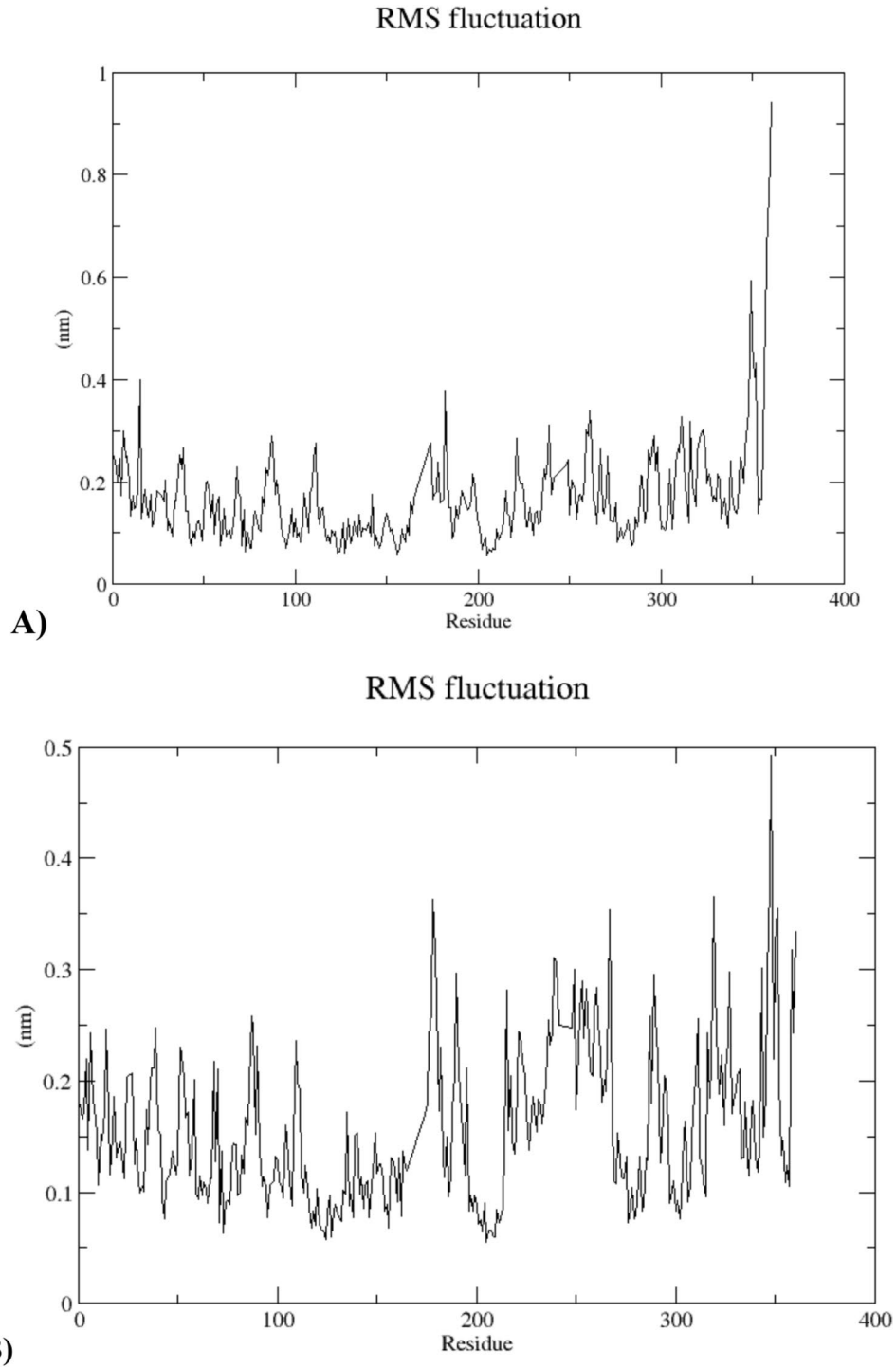

Fig. 24 RMSF graph of **A**) STAT3 **B**) STAT3-3MPAEMA

In the first 5,000 ps, the Ligand–Protein complex showed a sharp drop in Rg, suggesting quick structural compaction in the early phases of the simulation. In contrast to the single protein, the Rg values showed rather more noticeable oscillations during the remaining simulation period. Even though both graphs eventually stabilized within a comparable Rg range (2.06–2.08 nm), the fluctuation behavior raises the possibility that the Rg graph of protein–ligand complex has less internal stabilization or greater structural flexibility. When all results are considered, show that although both systems achieve a comparable level of compactness, the Rg graph of proteins seems to go through a slower but more stable conformational shift, whereas the Rg graph of protein–ligand complex compactions quickly but retains more dynamic flexibility (Fig. 25).

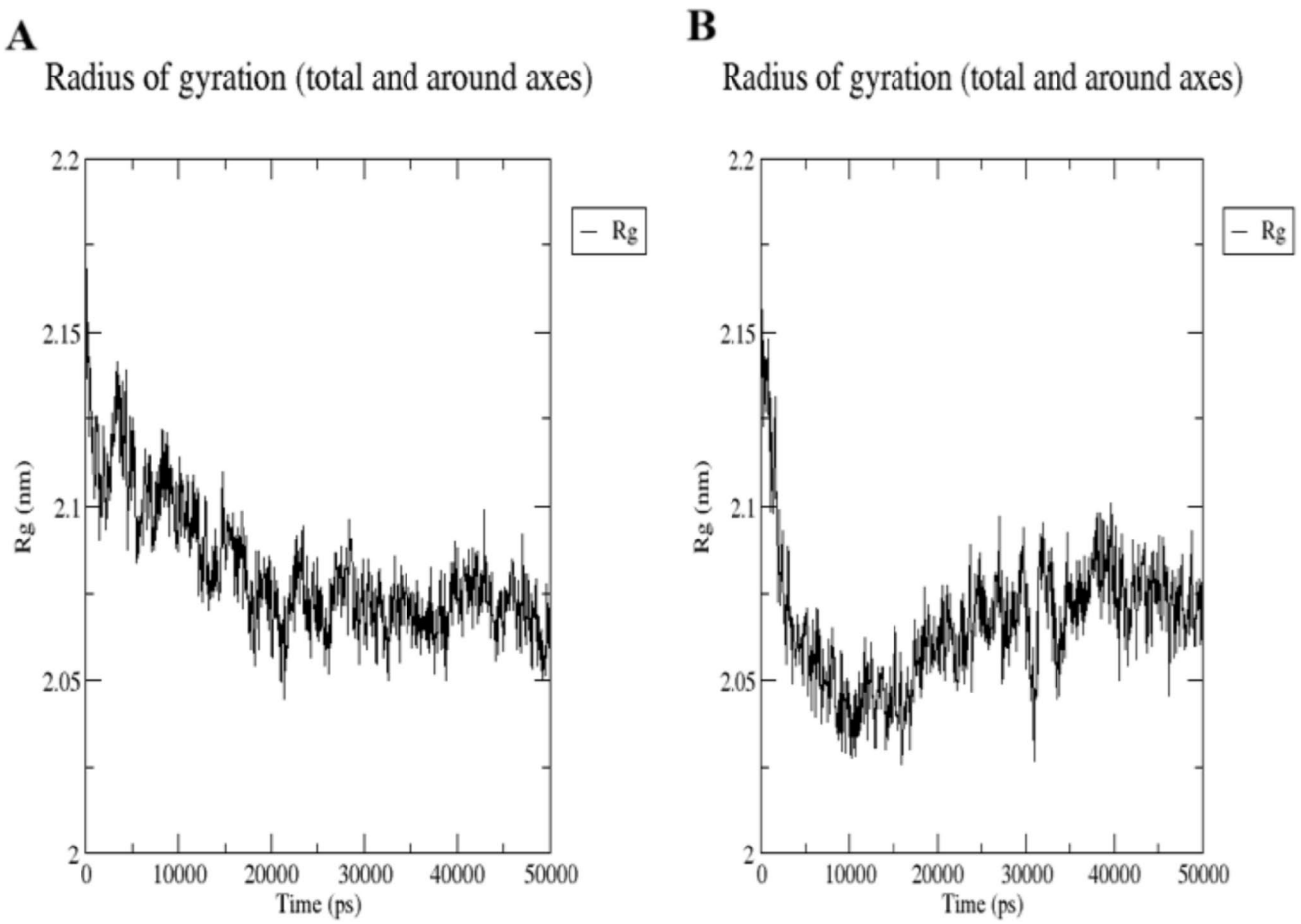

Fig. 25 Rg (Radius of Gyration) graphs **A**) Protein **B**) Protein–ligand complex

The protein and protein–ligand complex of solvent accessible surface area (SASA) plots show diverse patterns during the 50 ns simulation period, suggesting that the ligands interact with the systems differently (Fig. 26). The SASA value in the protein plot exhibits a sharp drop from about 190 nm^2 to about 165 nm^2 in the first 5 ns, followed by slow variations that stabilize about 160–170 nm^2. This pattern points to a reasonably stable conformational state after an initial structural rearrangement that is probably related to ligand binding or solvation effects. But the protein–ligand complex plot shows a more noticeable and quicker drop in SASA from about 190 nm^2 to 160 nm^2 in the first few nanoseconds, followed by the emergence of a more stable plateau phase. In contrast to the protein plot, the second system's smaller fluctuation range points to a more compact and stable complex development. All things considered, the Protein–ligand complex plot' sharper initial SASA decrease and less volatility suggest a stronger or more stable molecular connection, maybe because of tighter binding or less conformational flexibility. These results can result from variations in molecular packing efficiency or ligand affinity.

Molecular docking and molecular dynamics simulations of the MPAEMA molecule with its STAT3 target protein have demonstrated a stable and energetically advantageous contact between the two entities. The maintenance of the binding conformation and the stability of hydrogen bonds throughout the dynamic simulation corroborate the potential inhibitory impact of MPAEMA on STAT3. STAT3 is a crucial transcription factor that is persistently active in various cancer types and facilitates activities including tumor proliferation, survival, angiogenesis, and immune evasion [88, 89]. The association of MPAEMA with the active domain of STAT3 indicates that this factor may suppress the transcriptional function of STAT3, thereby diminishing the production of oncogenic genes such as Bcl-2, survivin, and VEGF [90–92]. Previous studies have demonstrated that small compounds targeting STAT3 inhibit tumor formation, perhaps with selectivity for cancer cells, given that STAT3 is more prevalent in tumor tissues than in normal tissues [93]. It is believed that a portion of MPAEMA's anticancer impact is mediated by the suppression of STAT3, and this effect may be selective.

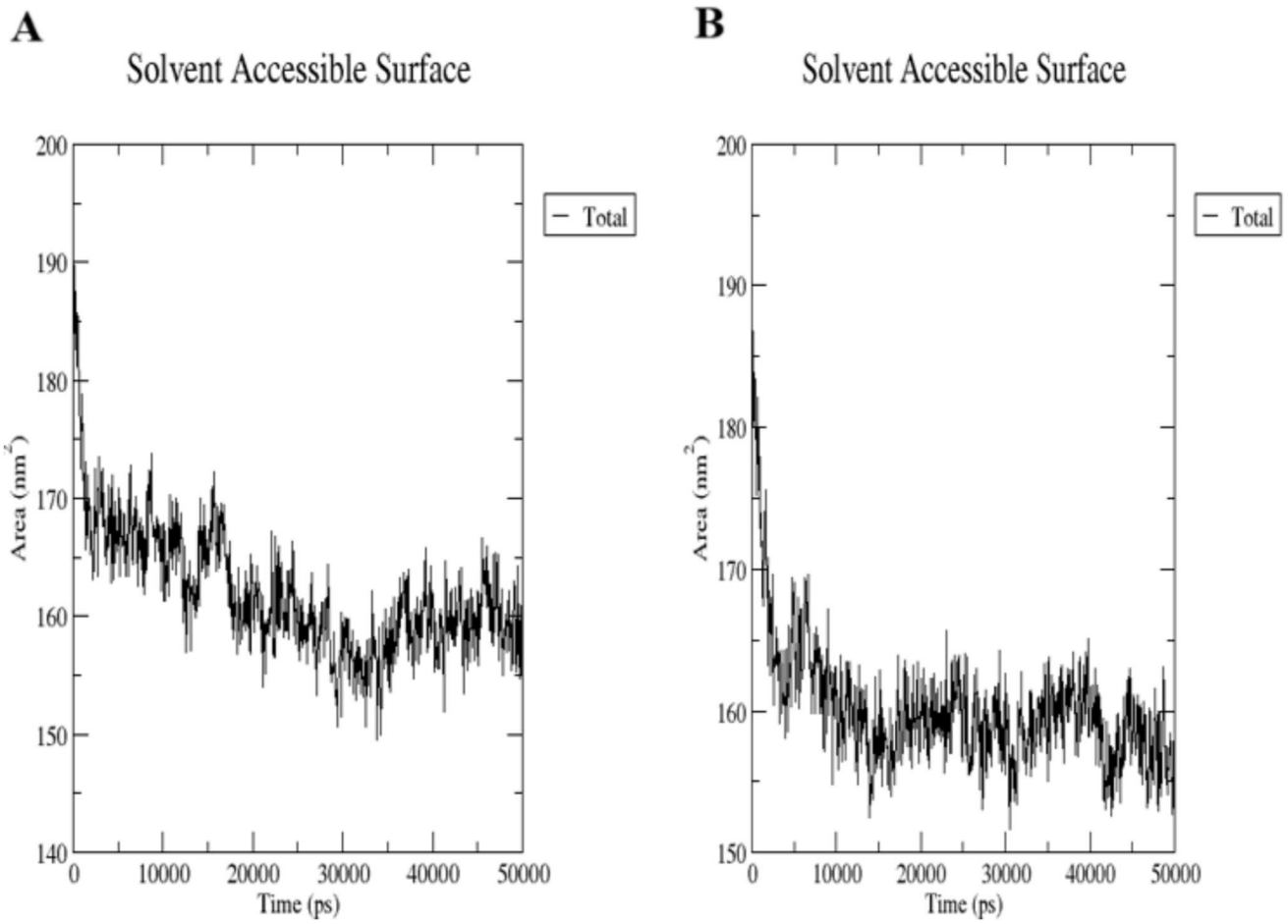

Fig. 26 SASA graphs **A**) Protein **B**) Protein–ligand complex

4 Conclusion

This study analyzes the synthesis, characterization, and computational evaluation of the novel compound 2-(3-methoxyphenylamino)−2-oxoethyl methacrylate (3MPAEMA), emphasizing its potential for diverse scientific and biomedical applications. Utilizing a combination of spectroscopic techniques and advanced computational methods—including Density Functional Theory (DFT), Natural Bond Orbital (NBO) analysis, and Frontier Molecular Orbital (FMO) analysis—we gained significant insights into the molecule's structural and electronic properties. These analyses revealed the compound's favorable stability, reactivity, and thermochemical characteristics, indicating its potential utility in areas such as polymer synthesis, tissue engineering, and drug delivery.

Toxicological evaluations using the Toxicity Estimation Software Tool (TEST) and QSAR-based methodologies indicated a moderate toxicity profile. Although 3MPAEMA showed low toxicity risks for critical endpoints such as carcinogenicity, mutagenicity, and immunotoxicity, we identified potential concerns such as nephrotoxicity, respiratory toxicity, and blood–brain barrier (BBB) permeability. Metabolic interaction with cytochrome P450 enzyme CYP3A4 suggests considerations for its pharmacokinetic behavior in drug development.

The study explored the therapeutic potential of 3MPAEMA as an inhibitor of the oncogenic transcription factor STAT3, a protein associated with several malignancies and inflammatory conditions. In silico docking and molecular dynamics (MD) simulations revealed strong binding affinity and stable interaction of 3MPAEMA at the SH2 domain of STAT3. These results suggest that 3MPAEMA holds promise as a STAT3-targeting agent in cancer therapy.

This study highlights the Multifaceted potential of 3MPAEMA across materials science and biomedical domains. Integrating experimental and computational approaches provided a solid framework for evaluating its physicochemical, biological, and pharmacological properties. However, we recommend further in vitro and in vivo studies to validate its therapeutic efficacy and safety profile before clinical translation.

Author Contributions NÇ and MHK and SYA wrote the main manuscript text, and also prepared figures and tables. All authors reviewed the manuscript.

Data Availability No datasets were generated or analysed during the current study.

Declarations

Ethical Approval This study did not include any humans or animals; therefore, we did not apply for ethical approval or register for clinical trials.

Conflict of interest The authors declare no competing interests.

Competing Interest The authors declare no competing financial interest.

References

1. S. Malviya, N. Malviya, *Medicinal Plants and Cancer Chemoprevention* (CRC Press, 2023)
2. K. Meena, S. Kumari, S. Mishra, M. Saini, J.S. Chauhan, *The role of genetics and hormones in women's health*. In Women's Health: A Comprehensive Guide to Common Health Issues in Women (Bentham Science Publishers, 2024), pp. 74–100. https://doi.org/10.2174/9789815256291124010 1
3. S. Ashique, M. Bhowmick, R. Pal, H. Khatoon, P. Kumar, H. Sharma, A. Garg, S. Kumar, U. Das, Multi drug resistance in Colorectal Cancer-approaches to overcome, advancements and future success. Advances in Cancer Biology - Metastasis **10**, 100114 (2024)
4. A. Hussein, K. Hussein, H. Babkair, M. Badawy, Anti-Cancer Medicins (Classification and Mechanisms of Action). Egyptian Dental Journal /Egyptian Dental Journal **70**(1), 147–164 (2024). https://doi.org/10.21608/edj.2023.234480.2708
5. B.İ Şimşek, H. Halıcı, E. Çadırcı, Molecularly Targeted Therapies in Breast Cancer: A Traditional Review. Fabad Journal of Pharmaceutical Sciences **49**(2), 435–448 (2024)
6. D. Datta, S. Sulthana, J. Strauss, A. Puri, S.P. Bandi, S. Singh, Reconnoitring signaling pathways and exploiting innovative approaches tailoring multifaceted therapies for skin cancer. Int. J. Pharm. **665**, 124719–124719 (2024)
7. Joshi, D. C., Sharma, A., Prasad, S., Singh, K., Kumar, M., Kajal Sherawat, Tuli, H. S., & Gupta, M. (2024). Novel therapeutic agents in clinical trials: emerging approaches in cancer therapy. *Discover Oncology*, 15(1). https://doi.org/10.1007/s12672-024-01195-7.
8. V. Tavares, I.S. Marques, I. Guerra, J. Assis, D. Pereira, R. Medeiros, Paradigm Shift: A Comprehensive Review of Ovarian Cancer Management in an Era of Advancements. Int. J. Mol. Sci. **25**(3), 1845–1845 (2024). https://doi.org/10.3390/ijms25031845
9. R.P. Verma, C. Hansch, Matrix metalloproteinases (MMPs): Chemical–biological functions and (Q)SARs. Bioorg. Med. Chem. **15**(6), 2223–2268 (2007). https://doi.org/10.1016/j.bmc.2007.01.011
10. H. Xiong, J. Hong, W. Du, Y. Lin, L. Ren, Y. Wang, W. Su, J. Wang, Y. Cui, Z. Wang, J.-Y. Fang, Roles of STAT3 and ZEB1 Proteins in E-cadherin Down-regulation and Human Colorectal Cancer Epithelial-Mesenchymal Transition. J. Biol. Chem. **287**(8), 5819–5832 (2011). https://doi.org/10.1074/jbc.m111.295964
11. T. Wang, G. Niu, M. Kortylewski, L. Burdelya, K. Shain, S. Zhang, R. Bhattacharya, D. Gabrilovich, R. Heller, D. Coppola, W. Dalton, R. Jove, D. Pardoll, H. Yu, Regulation of the innate and adaptive immune responses by Stat-3 signaling in tumor cells. Nat. Med. **10**(1), 48–54 (2003). https://doi.org/10.1038/nm976
12. Hu, Y., Dong, Z., & Liu, K. (2024). Unraveling the complexity of STAT3 in cancer: molecular understanding and drug discovery. *Journal of Experimental & Clinical Cancer Research*, *43*(1). https://doi.org/10.1186/s13046-024-02949-5
13. T. Aziz, W. Li, J. Zhu, B. Chen, Developing multifunctional cellulose derivatives for environmental and biomedical applications: Insights into modification processes and advanced material properties. Int. J. Biol. Macromol. **278**, 134695–134695 (2024). https://doi.org/10.1016/j.ijbiomac.2024.134695
14. S.M. Mawazi, M. Kumar, N. Ahmad, Y. Ge, S. Mahmood, Recent Applications of Chitosan and Its Derivatives in Antibacterial, Anticancer, Wound Healing, and Tissue Engineering Fields. Polymers **16**(10), 1351 (2024). https://doi.org/10.3390/polym16101351
15. V. Çoban, N. Çankaya, S.Y. Azarkan, New oxomethacrylate and acetamide: synthesis, characterization, and their computational approaches: molecular docking, molecular dynamics, and ADME analyses. Drug Chem. Toxicol. **47**(6), 1175–1184 (2024). https://doi.org/10.1080/01480545.2024.2349651
16. S. Şahin, A New Molecular Structure and Computational Analyses: DFT Studies, NLO Properties, ADMET Predictions, Biological Targets, and Docking Experiments. Polycyclic Aromat. Compd. **44**(6), 4029–4043 (2023). https://doi.org/10.1080/10406638.2023.2244630
17. J. Eberhardt, D. Santos-Martins, A.F. Tillack, S. Forli, AutoDock Vina 1.2. 0: New docking methods, expanded force field, and python bindings. Journal of Chemical Information and Modeling **61**(8), 3891–3898 (2021)
18. O. Trott, A.J. Olson, AutoDock Vina: improving the speed and accuracy of docking with a new scoring function, efficient optimization, and multithreading. J. Comput. Chem. **31**(2), 455–461 (2010)
19. S. Murail, S.J. De Vries, J. Rey, G. Moroy, P. Tufféry, SeamDock: an interactive and collaborative online docking resource to assist small compound molecular docking. Front. Mol. Biosci. **8**, 716466 (2021)
20. P. Tufféry, S. Murail, *samuelmurail/docking_py: Docking_py, a python library for ligand protein docking* (Zenodo, Paris, France, 2020), p.10
21. D.V.D. Spoel, E. Lindahl, B. Hess, G. Groenhof, A.E. Mark, H.J.C. Berendsen, GROMACS: Fast, flexible, and free. J. Comput. Chem. **26**(16), 1701–1718 (2005). https://doi.org/10.1002/jcc.20291
22. M.J. Abraham, T. Murtola, R. Schulz, S. Páll, J.C. Smith, B. Hess, E. Lindahl, GROMACS: High performance molecular simulations through multi-level parallelism from laptops to supercomputers. SoftwareX **1**, 19–25 (2015)
23. K. Jurowski, A. Krośniak, Prediction of key toxicity endpoints of AP-238 a new psychoactive substance for clinical toxicology and forensic purposes using in silico methods. Sci. Rep. **14**(1), 28977 (2024)
24. N. Abad, P. Akhileshwari, M.S. Aljohani, H.Y. Alharbi, S. Saffour, J.T. Mague, E.M. Essassi, Y. Ramli, F.H. Al-Ostoot, Molecular drug design, theoretical, experimental approaches and new framework of novel oxazol dihydroquinoxaline (ODQ): Efficient synthesis, crystallographic, computational investigation, DFT calculation, ADME analysis and antiangiogenic molecular docking. J. Mol. Struct. **1321**, 139762 (2025). https://doi.org/10.1016/j.molstruc.2024.139762
25. W. Kohn, L.J. Sham, Self-consistent equations including exchange and correlation effects. Phys. Rev. **140**(4A), A1133 (1965)
26. S. Santhosh, P. Chakkaravarthy, D. Babu, G. Ramalingam, V. Vetrivelan, Evaluation of electronic properties, molecular profiling, bioactivity score, anti-microbial activity and quantum

computational studies on methyl (2E)-2-{[N-(2-formylphenyl) (4-methylbenzene)sulfonamide]methyl}-3-[4-(propan-2-yl)phenyl]prop-2-enoate. Chemical Physics Impact **8**, 100511–100511 (2024). https://doi.org/10.1016/j.chphi.2024.100511
27. R. Gao, L. Zhu, Q. Zhang, W. Wang, Atmospheric oxidation mechanism and kinetic studies for OH and NO3 radical-initiated reaction of methyl methacrylate. Int. J. Mol. Sci. **15**(3), 5032–5044 (2014)
28. J.J. Belbruno, The application of effective core potentials in heavy atom molecules: A study of small gold clusters and molecules as a function of theoretical method. Heteroat. Chem. **9**(7), 651–657 (1998)
29. W. Li, H. Dong, J. Ma, S. Li, Structures and Spectroscopic Properties of Large Molecules and Condensed-Phase Systems Predicted by Generalized Energy-Based Fragmentation Approach. Acc. Chem. Res. **54**(1), 169–181 (2020). https://doi.org/10.1021/acs.accounts.0c00580
30. E. Kavitha, N. Sundaraganesan, S. Sebastian, M. Kurt, Molecular structure, anharmonic vibrational frequencies and NBO analysis of naphthalene acetic acid by density functional theory calculations. Spectrochim. Acta Part A Mol. Biomol. Spectrosc. **77**(3), 612–619 (2010). https://doi.org/10.1016/j.saa.2010.06.034
31. S.G. Hernández-Rizo, E.R. Larios-Durán, M. Bárcena-Soto, Frequency response of Gibbs free energy and enthalpy changes of electrochemical systems analyzed as thermometric transfer functions. J. Solid State Electrochem. **27**(11), 3177–3188 (2023)
32. R. Ohmura, S. Alavi, Zero-point energy effects on the stability of water clusters: Implications on the uptake of hydrogen isotope substituted water on ice and clathrate hydrate phases. AIP Advances **14**(3), 035142 (2024). https://doi.org/10.1063/5.0186940
33. N. Yasarawan, K. Thipyapong, S. Sirichai, V. Ruangpornvisuti, Fundamental insights into conformational stability and orbital interactions of antioxidant (+)-catechin species and complexation of (+)-catechin with zinc (II) and oxovanadium (IV). J. Mol. Struct. **1047**, 344–357 (2013). https://doi.org/10.1016/j.molstruc.2013.05.038
34. V.J. Reeda, S. Sakthivel, P. Divya, S. Javed, V.B. Jothy, Conformational stability, quantum computational (DFT), vibrational, electronic and non-covalent interactions (QTAIM, RDG and IGM) of antibacterial compound N-(1-naphthyl) ethylenediamine dihydrochloride. J. Mol. Struct. **1298**, 137043 (2024)
35. S.A. Halim, A.B. El-Meligy, A.M. El-Nahas, S.H. El-Demerdash, DFT study, and natural bond orbital (NBO) population analysis of 2-(2-Hydroxyphenyl)-1-azaazulene tautomers and their mercapto analouges. Sci. Rep. **14**(1), 219 (2024)
36. T. Lu, A comprehensive electron wavefunction analysis toolbox for chemists. Multiwfn. J. Chem. Phys. **161**(8), 082503 (2024). https://doi.org/10.1063/5.0216272
37. Y. Takeda, Modulating the Photophysical Properties of Twisted Donor–Acceptor–Donor π-Conjugated Molecules: Effect of Heteroatoms, Molecular Conformation, and Molecular Topology. Acc. Chem. Res. **57**(15), 2219–2232 (2024). https://doi.org/10.1021/acs.accounts.4c00353
38. L.G. Zhuo, W. Liao, Z.X. Yu, A frontier molecular orbital theory approach to understanding the Mayr equation and to quantifying nucleophilicity and electrophilicity by using HOMO and LUMO energies. Asian Journal of Organic Chemistry **1**(4), 336–345 (2012)
39. F. Ak, M.H. Kebiroglu, Theoretical Investigation of the Chemical Reactivity of Acrylic Acid Molecules: A DFT Study with UV-Vis, NMR, and FT-IR Spectroscopy Using STO-3G Basis Set. Yüzüncü Yıl Üniversitesi Fen Bilimleri Enstitüsü Dergisi **29**(2), 438–446 (2023)
40. L. Zhao, B. Yuan, L. Gong, H. Wang, Q. Ran, L. Qin, J. Liu, L. Zhang, K. Li, G. Liang, L. Li, Q. Xie, Insight into the molecular structure construction and pyrolysis mechanism simulation of typical carbonaceous feedstocks for the rapid design and preparation of porous carbon-based materials. Fuel **379**, 132893 (2025). https://doi.org/10.1016/j.fuel.2024.132893
41. K.W. Qadir, M.D. Mohammadi, H.Y. Abdullah, Adsorption mechanism of CO, CO2, NO, NO2, and SO2 gases onto AlNNT (m, n) _k,(m= 5, 7; n= 0, 5, 7; k= 3–9). Mater. Sci. Semicond. Process. **185**, 108973 (2025)
42. K-J. Ylivainio, A. Sufyan, J.A. Larsson, A quantitative relationship between electron localization function and the strength of physical binding. J. Phys. Condens. Matter **37**(20) 205502 (2025). https://doi.org/10.1088/1361-648X/adcc70
43. N. Kanagathara, G. Dhanalakshmi, E. Mohanapriya, Palani Manikandan, A.K. Mohanakrishnan, V. Sabari, Dabora Vincy, V. Ragavendran, S. Aravindhan, Structural and computational insights into a benzene sulfonamide derivative: Hirshfeld surface, energy framework, optical, NBO, electronic and biological properties. J. Mol. Struct. **1330,** 141347 (2025). https://doi.org/10.1016/j.molstruc.2025.141347
44. C. Zhang, Z. Zhou, M. Xi, H. Ma, J. Qin, H. Jia, Molecular modeling to elucidate the dynamic interaction process and aggregation mechanism between natural organic matters and nanoplastics. Eco-Environment & Health **4**(1), 100122 (2025). https://doi.org/10.1016/j.eehl.2024.08.004
45. Z. Geng, C. Ding, J. Hu, J.D. Ampah, C. Jin, H. Liu, Revealing a new mechanism of stable intersolubility of methanol-n-heptane blended fuel assisted by co-solvents at the microscopic molecular level: Insights and validation from quantum chemical simulation. J. Mol. Liq. **417**, 126626 (2025)
46. Q. Mu, G. Jiang, L. Chen, H. Zhou, D. Fourches, A. Tropsha, B. Yan, Chemical basis of interactions between engineered nanoparticles and biological systems. Chem. Rev. **114**(15), 7740–7781 (2014)
47. S. Sun, Y. Zhang, X. Shi, W. Sun, C. Felser, W. Li, G. Li, From Charge to Spin: An In-Depth Exploration of Electron Transfer in Energy Electrocatalysis. Adv. Mater. **36**(37), 2312524 (2024). https://doi.org/10.1002/adma.202312524
48. J. Liang, P. Zhen, P. Gan, Y. Li, M. Tong, W. Liu, DFT calculation of nonperiodic small molecular systems to predict the reaction mechanism of advanced oxidation processes: challenges and perspectives. ACS ES&T Engineering **4**(1), 4–18 (2023)
49. V. Rustagi, S.R. Gupta, A. Singh, I.K. Singh, Beyond trial and error: Leveraging advanced software for Therapeutic discovery. Chemical Biology Letters **12**(1), 1251–1251 (2025)
50. N. Elangovan, S. Sowrirajan, N. Arumugam, B. Rajeswari, S. Mathew, C.G. Priya, ... & S.M. Mahalingam, Theoretical investigation on solvents effect in molecular structure (TD-DFT, MEP, HOMO-LUMO), topological analysis and molecular docking studies of n-(5-((4-ethylpiperazin-1-yl) methyl) pyridin-2-yl)-5-fluoro-4-(4-fluoro-1-isopropyl-2-methyl-1H-benzo [d] imidazol-6-yl) pyrimidin-2-amine. Polycycl. Aromat. Compd. **44**(7), 4467–4490 (2024). https://doi.org/10.1080/10406638.2023.2254896
51. A. Suhta, S. Saral, U. Çoruh, S. Karakuş, E..M.. Vazquez-Lopez, Synthesis, Single Crystal X-Ray, Hirshfeld Surface Analysis and DFT Calculation Based NBO, HOMO–LUMO, MEP, ECT and Molecular Docking Analysis of N′-[(2, 6-Dichlorophenyl) Methylidene]-2-{[3-(Trifluoromethyl) Phenyl] Amino} Benzohydrazide. J. Struct. Chem. **65**(1), 196–215 (2024). https://doi.org/10.1134/S0022476624010189
52. H. Kebiroglu, Ö. Büyük, N. Bulut, Investigation of propyphenazone molecule by quantum chemical methods. Journal of Physical Chemistry and Functional Materials **5**(2), 40–48 (2022)
53. J.G. Vinter, A. Davis, M.R. Saunders, Strategic approaches to drug design. I. An integrated software framework for molecular modelling. J. Comput. Aided Mol. Des. **1**, 31–51 (1987)
54. F.N.O. Bruce, D. Zhang, X. Bai, S. Song, F. Wang, Q. Chu, D. Chen, Y. Li, Machine learning predictions of thermochemical

properties for aliphatic carbon and oxygen species. Fuel **384**, 133999 (2025). https://doi.org/10.1016/j.fuel.2024.133999
55. G. Andriani, G. Pio, E. Salzano, C. Vianello, P. Mocellin, Evaluating the thermal stability of chemicals and systems: A review. The Canadian Journal of Chemical Engineering **103**(1), 42–62 (2025). https://doi.org/10.1002/cjce.25422
56. S. Haider, A. Haider, S.U.-D. Khan, *Density Functional Theory - New Perspectives and Applications* (In IntechOpen eBooks, IntechOpen, 2023). https://doi.org/10.5772/intechopen.104137
57. M.T. Hossain, F-T. Zahra, M.M. Hasan, S. Swargo, R.A.A. Dhroobo, M.R. Al Amin, F.M.A. Sieam, S.T. Disha, M.R. Islam, First-principles insights into the structural, mechanical, electronic, optical, and thermophysical properties of XSrBr3 (X= Na, Ga, and Tl) perovskites: Implications for optoelectronic applications. Mater. Sci. Semicond. Process. **182,** 108694 (2024). https://doi.org/10.1016/j.mssp.2024.108694
58. T. Kim, G. Shin, T. Park, M. Kim, Molecular Design Leveraging Non-Covalent Interactions for Efficient Light-Emitting Organic Small Molecules. Adv. Funct. Mater. **35**(2), 2412267 (2024). https://doi.org/10.1002/adfm.202412267
59. S. Chen, Q. Mao, H. Cheng, W. Tai, RNA-Binding Small Molecules in Drug Discovery and Delivery: An Overview from Fundamentals. J. Med. Chem. **67**(18), 16002–16017 (2024)
60. A.I. Odugbemi, C. Nyirenda, A. Christoffels, S.A. Egieyeh, Artificial intelligence in antidiabetic drug discovery: The advances in QSAR and the prediction of α-glucosidase inhibitors. Comput. Struct. Biotechnol. J. **23,** 2964–2977 (2024). https://doi.org/10.1016/j.csbj.2024.07.003
61. N. Çankaya, M.H. Kebiroğlu, M.M. Temüz, A comprehensive study of experimental and theoretical characterization and in silico toxicity analysis of new molecules. Drug Chem. Toxicol. **47**(6), 1226–1240 (2024)
62. M. Boutalaka, S. El Bahi, M. Alaqarbeh, M.A. El Alaouy, Y. Koubi, K. El Khatabi, H. Maghata, M. Bouachrinea, T. Lakhlifi, Computational investigation of imidazo[2,1-b]oxazole derivatives as potential mutant BRAF kinase inhibitors: 3D-QSAR, molecular docking, molecular dynamics simulation, and ADMETox studies. J. Biomol. Struct. Dyn. **42**(10), 5268–5287 (2023). https://doi.org/10.1080/07391102.2023.2233629
63. L. El Mchichi, A. El Aissouq, R. Kasmi, A. Belhassan, R. El-Mernissi, A. Ouammou, T. Lakhlifi, M. Bouachrine, In silico design of novel Pyrazole derivatives containing thiourea skeleton as anti-cancer agents using: 3D QSAR, Drug-Likeness studies, ADMET prediction and molecular docking. Materials Today: Proceedings. **45**, 7661–7674 (2021). https://doi.org/10.1016/j.matpr.2021.03.152
64. B. Mahajan, P. Gawarkar-Patil, P. Adnaik, N. Bagade, P. Gondhale-Karpe, S. Manwatkar, S. Patil, Applications of Computational Tools in the Prediction of Toxicity, in *Biosystems, Biomedical & Drug Delivery Systems: Characterization, Restoration and Optimization*. (Singapore, Springer Nature Singapore, 2024), pp.311–326
65. D. Faeni, Green Practices and Employees' Performance: The Mediating Roles of Green Human Resources Management Policies and Knowledge Development. Journal of Infrastructure, Policy and Development **8**(8), 4924 (2024)
66. R.L. Siegel, A.N. Giaquinto, A. Jemal, Cancer statistics, 2024. CA: A Cancer Journal for Clinicians **74**(1), 12–49 (2024)
67. E. Belghalia, F. Elbamtari, M. Jawi, A. Guendouzi, A. Sbai, M. Choukrad, T. Lakhlifi, M. Bouachrine, Pyrazole-benzimidazole derivatives targeting MCF-7 breast cancer cells as potential antiproliferative agents. 3D QSAR and In-silico investigations via molecular docking and molecular dynamics simulations. Comput. Biol. Med. **189,** 109969 (2025). https://doi.org/10.1016/j.compbiomed.2025.109969
68. S. El Rhabori, M. Alaqarbeh, Y. El Allouche, L. Naanaai, A. El Aissouq, M. Bouachrine, S. Chtita, F. Khalil, Exploring innovative strategies for identifying anti-breast cancer compounds by integrating 2D/3D-QSAR, molecular docking analyses, ADMET predictions, molecular dynamics simulations, and MM-PBSA approaches. J. Mol. Struct. **1320**, 139500 (2025). https://doi.org/10.1016/j.molstruc.2024.139500
69. K. Lindorff-Larsen, S. Piana, K. Palmo, P. Maragakis, J.L. Klepeis, R.O. Dror, D.E. Shaw, Improved side-chain torsion potentials for the Amber ff99SB protein force field. Proteins: Structure, Function, and Bioinformatics **78**(8), 1950–1958 (2010)
70. P. Bjelkmar, P. Larsson, M.A. Cuendet, B. Hess, E. Lindahl, Implementation of the CHARMM force field in GROMACS: analysis of protein stability effects from correction maps, virtual interaction sites, and water models. J. Chem. Theory Comput. **6**(2), 459–466 (2010)
71. S. Yalçınkaya, S.Y. Azarkan, A.G.K. Çakmakçı, Determination of the effect of L. plantarum AB6-25, L. plantarum MK55 and S. boulardii T8-3C microorganisms on colon, cervix, and breast cancer cell lines: Molecular docking, and molecular dynamics study. Journal of Molecular Structure **1261**, 132939 (2022)
72. C. Oostenbrink, A. Villa, A.E. Mark, W.F. Van Gunsteren, A biomolecular force field based on the free enthalpy of hydration and solvation: the GROMOS force-field parameter sets 53A5 and 53A6. J. Comput. Chem. **25**(13), 1656–1676 (2004)
73. M.F. Khan, G. Verma, P. Alam, M. Akhter, M.A. Bakht, S.M. Hasan, M. Shaquiquzzaman, M.M. Alam, Dibenzepinones, dibenzoxepines and benzosuberones based p38α MAP kinase inhibitors: Their pharmacophore modelling, 3D-QSAR and docking studies. Comput. Biol. Med. **110**, 175–185 (2019). https://doi.org/10.1016/j.compbiomed.2019.05.023
74. S. Babiyana, V. Balachandran, N. Thirughanasambantham, A. Viji, B. Narayana, V.V. Salian, N.S. Alharbi, J.M. Khaled, Spectroscopic characterizations, RDG and docking study of 2-[3-(4-chlorophenyl)-5-(4-(propane-2-yl) phenyl)-4,5-dihydro-1H pyrozol-1-yl]-4-(4-fluorophenyl)-1,3-thiazole. Zeitschrift für Physikalische Chemie **238**(10), 1887–1914 (2024). https://doi.org/10.1515/zpch-2024-0598
75. H. Kebiroglu, F. Ak, Molecular Structure, Geometry Properties, HOMO-LUMO, and MEP Analysis of Acrylic Acid Based on DFT Calculations. Journal of Physical Chemistry and Functional Materials **6**(2), 92–100 (2023)
76. Y. Gong, X. Chen, W. Wu, Application of fourier transform infrared (FTIR) spectroscopy in sample preparation: Material characterization and mechanism investigation. Advances in Sample Preparation **11**, 100122 (2024)
77. D. Barrena-Espés, J. Munárriz, Á.M. Pendás, How electrons still guard the space: Electron number distribution functions based on QTAIM∩ ELF intersections. J. Chem. Phys. **160**(14), 144106 (2024). https://doi.org/10.1063/5.0199318
78. D.T Agi, K.D Jones, M.J Watson, H.G Lynch, M. Dougher, X. Chen, M.N Carlozo, A.W Dowling, Computational toolkits for model-based design and optimization. Curr. Opin. Chem. Eng. **43**,100994 (2024). https://doi.org/10.1016/j.coche.2023.100994
79. A. Cherkasov, E.N. Muratov, D. Fourches, A. Varnek, I.I. Baskin, M. Cronin, J. Dearden et al., QSAR modeling: where have you been? Where are you going to?. J. Med. Chem. **57**(12), 4977–5010 (2014). https://doi.org/10.1021/jm4004285
80. M. Monnishkaran, K. Jaganathan, L. Shanmugam. Deep learning-based multimodal fusion approach for predicting acute dermal toxicity. J. Chem. Inf. Model. **65**, 7540–7553 (2025). https://doi.org/10.1021/acs.jcim.5c01128
81. Y. El Masaoudy, K. Tabti, Y. Koubi, H. Maghat, T. Lakhlifi, M. Bouachrine, In silico design of new pyrimidine-2, 4-dione derivatives as promising inhibitors for HIV Reverse Transcriptase-associated RNase H using 2D-QSAR modeling and (ADME/Tox)

properties. Mor. J. Chem. **11**(2), 300-317 (2023). https://revues.imist.ma/index.php/morjchem
82. K. Tabti, A. Sbai, H. Maghat, T. Lakhlifi, M. Bouachrine, Computational assessment of the reactivity and pharmaceutical potential of novel triazole derivatives: an approach combining DFT calculations, molecular dynamics simulations, and molecular docking. Arab. J. Chem. **17**(1), 105376 (2024). https://revues.imist.ma/index.php/morjchem
83. L. El Mchichi, K. Tabti, R. Kasmi, R. El-Mernissi, A. El Aissouq, F. En-nahli, A. Belhassan, T. Lakhlifi, M. Bouachrine, 3D-QSAR study, docking molecular and simulation dynamic on series of benzimidazole derivatives as anti-cancer agents. J. Indian Chem. Soc. **99**(9), 100582 (2022). https://doi.org/10.1016/j.jics.2022.100582
84. Z. He, B. Song, M. Zhu, J. Liu, Comprehensive pan-cancer analysis of STAT3 as a prognostic and immunological biomarker. Scientific reports **28,13**(1), 5069 (2023)
85. Z. Qureshy, H. Li, Y. Zeng, J. Rivera, N. Cheng, C.N. Peterson, J.R. Grandis, STAT3 activation as a predictive biomarker for ruxolitinib response in head and neck cancer. Clinical Cancer Research **1;28**(21), 4737–4746 (2022)
86. L. Martínez, Automatic identification of mobile and rigid substructures in molecular dynamics simulations and fractional structural fluctuation analysis. PLoS ONE **10**(3), e0119264 (2015)
87. S.K. Paul, M. Saddam, K.A. Rahaman, J.G. Choi, S.S. Lee, M. Hasan, Molecular modeling, molecular dynamics simulation, and essential dynamics analysis of grancalcin: An upregulated biomarker in experimental autoimmune encephalomyelitis mice. Heliyon **23,8**(10), e11232 (2022)
88. H. Yu, D. Pardoll, R. Jove, STATs in cancer inflammation and immunity: a leading role for STAT3. Nat. Rev. Cancer **9**(11), 798–809 (2009). https://doi.org/10.1038/nrc2734
89. D.E. Johnson, R.A. O'Keefe, J.R. Grandis, Targeting the IL-6/JAK/STAT3 signalling axis in cancer. Nat. Rev. Clin. Oncol. **15**(4), 234–248 (2018)
90. P. Gao, N. Niu, T. Wei, H. Tozawa, X. Chen, C. Zhang, J. Zhang, Y. Wada, C. M. Kapron, J. Liu, The roles of signal transducer and activator of transcription factor 3 in tumor angiogenesis. Oncotarget **8**(40), 69139–69161 (2017). https://doi.org/10.18632/oncotarget.19932
91. S.H. Chen, D.A. Murphy, W. Lassoued, G. Thurston, M.D. Feldman, W.M. Lee, Activated STAT3 is a mediator and biomarker of VEGF endothelial activation. Cancer Biol. Ther. **7**(12), 1994–2003 (2008). https://doi.org/10.4161/cbt.7.12.6967
92. J.H. Choi, M.J. Ahn, C.K. Park, H.X. Han, S.J. Kwon, Y.Y. Lee, I.S. Kim, Phospho-Stat3 expression and correlation with VEGF, p53, and Bcl-2 in gastric carcinoma using tissue microarray. APMIS : acta pathologica, microbiologica, et immunologica Scandinavica **114**(9), 619–625 (2006). https://doi.org/10.1111/j.1600-0463.2006.apm_401.x
93. K. Siddiquee, S. Zhang, W.C. Guida, M.A. Blaskovich, B. Greedy, H.R. Lawrence, M.L.R. Yip, J. Turkson, Selective chemical probe inhibitor of Stat3, identifiedthrough structure-based virtual screening, inducesantitumor activity. Proc. Natl. Acad. Sci. **104**(18), 7391–7396 (2007). https://doi.org/10.1073/pnas.0609757104